

Peak factor statistics of wind effects for hyperbolic paraboloid roofs

Fabio Rizzo¹, Michele Barbato², Vincenzo Sepe³

¹ CRIACIV (Inter-University Research Centre for Building Aerodynamics and Wind Engineering), Italy, fabio.rizzo@unich.it

² Louisiana State University, 3230B Patrick F. Taylor Hall, Baton Rouge, LA 70803, USA, mbarbato@lsu.edu (corresponding author)

³ University "G. D'Annunzio" of Chieti-Pescara, Viale Pindaro 42, 65127 Pescara, Italy, v.sepe@unich.it.

Abstract

This paper investigates the statistics of the pressure coefficients and their peak factors in hyperbolic paraboloid roofs that are commonly used in tensile structures. The experimental peak factor statistics, estimated using pressure coefficient time histories experimentally measured in wind tunnel tests, were compared with the corresponding peak factor statistics estimated through the use of six analytical models available in the literature, namely the Davenport, classical Hermite, revised Hermite, modified Hermite, Translated-Peak-Process (TPP), and Liu's models. The basic assumption of the TPP model, i.e., that the pressure coefficient local peaks follow a Weibull distribution, was validated and was used to estimate analytically the peak factors' quantiles. Different time history durations and different error measures were also considered. The non-Gaussian properties of the pressure coefficient processes were characterized at different roof locations for different wind angles of attack. It was found that: (1) the region of non-Gaussianity is significantly affected by the wind angle; (2) as expected, the Davenport model underestimates the peak factor mean and standard deviation in regions of high non-Gaussianity; (3) the modified Hermite model provides the best estimates overall of the peak factor mean; and (4) the TPP model provides the best estimates overall of the peak factor standard deviation. In addition, the modified root mean squared error was found to provide the most reliable assessment of the analytical models' accuracy among the different error measures considered in this study.

Keywords:

Wind-induced pressure, wind peak factor, hyperbolic paraboloid roofs, probabilistic wind effect modeling, non-Gaussian stochastic processes, wind tunnel tests.

28 **1 Introduction**

29 Tensile structures are widely used for hyperbolic paraboloid roofs (HPRs). This structural typology is
30 frequently used for multi-functional buildings that require large interior open spaces [1], since they allow
31 covering extremely large spans (up to 150 m, as for example The Khan Shatyr Entertainment Centre in
32 Kazakhstan, completed in 2010) without intermediate pillars in a cost-effective manner. In addition, they
33 are lighter than other structural typologies for similar spans and, thus, permits a wider selection of design
34 solutions.

35 These structures present the unique feature that their load-bearing elements (i.e., cables and membranes)
36 sustain pure tension and, thus, resist very efficiently external loads [2], [3], [4]). These load-bearing
37 elements are very flexible and generally experience large deflections. Thus, the initial structural
38 equilibrium configuration needs to be optimized through the appropriate distribution of permanent loads
39 and a careful selection of the geometric shape. The most commonly used shape for tensile structures is
40 the hyperbolic paraboloid, which has been employed in many structures around the world, e.g., the
41 Olympiastadion in Munich, Germany (designed by Otto Frei and completed in 1968) and the Denver
42 Union Station roof in Denver, CO (USA) (completed in 2013). The hyperbolic paraboloid is an
43 elementary double curvature surface, nowadays usually realized by means of two series of parallel cables,
44 one series oriented upward and the other downward. For load combinations controlled by gravity loads
45 (e.g., self-weight, dead and snow loads), the upward cables act as load-bearing cables, whereas the
46 downward cables are stabilizing cables. However, under suction due to wind loads, the upward cables
47 provide the stabilizing action, whereas the downward cables resist the wind loads.

48 Because of their lightness and deformability, the stability of tensile structures and in particular of
49 hyperbolic paraboloid cable nets is extremely sensitive to their aerodynamic and aeroelastic response
50 under wind actions. However, knowledge of these aerodynamic and aeroelastic behaviors is limited [2].

51 In addition, existing technical codes provide design guidelines only for static loading conditions and/or

52 temporary structures [5], [6], [7]. These code prescriptions are backed up by several manuals of practice,
53 which examine in depth several aspects related to the design of tensioned fabric roofs [8], [9]. In this
54 context, the European Network for Membrane Structures “TensiNet” developed the TensiNet Design
55 Guide [10], which is widely considered the state-of-the-art guide for the design of tensile structures and
56 also provides a few examples of aerodynamic wind actions on tensile structures [4].

57 It is noted here that HPRs have been used in the past also for low-flexibility shell structures made of light
58 reinforced concrete (e.g., the Olympic Saddledome in Calgary and several buildings designed by Mexican
59 architect Felix Candela [11]), and for medium-flexibility lattice structures constructed with plywood [12].
60 For these stiffer structural typologies, the aerodynamic behavior is predominant, whereas the aeroelastic
61 behavior has a smaller influence on the structural design. For flexible HPRs consisting of tensile
62 structures, both aerodynamic and aeroelastic behaviors are equally important and their characterization
63 for design purposes requires an iterative two-phase approach in which the results of two separate analyses
64 (performed numerically or experimentally in wind tunnels) are interdependent [13]. However, the
65 pressure coefficients can be estimated accurately using rigid models in wind tunnel tests even for flexible
66 HPRs, since the deflections of well-designed structures need to satisfy code requirements and are
67 generally too small to affect the pressure coefficients [14].

68 The importance of the aerodynamic behavior of HPRs has been recognized in a few recent studies that
69 investigated the dynamic behavior [14], [15], [16], [17] and the distribution of pressure coefficients on
70 different geometries [18], [19], [20], [21], [22], [23], [24], [25], [26]. It is noteworthy that peak pressure
71 coefficients (usually expressed in terms of peak factors) are crucial to estimate peak loads [27], which for
72 this type of structure could be related to local and global critical conditions. In addition, modern
73 performance-based reliability design approaches require the accurate estimation of extreme wind loads
74 and their distribution [28], [29], [30].

75 In principle, the peak factor's distribution can be obtained based on the classical extreme value theory
76 [31]. If the process is Gaussian, the Davenport equations provide satisfactory estimates of the mean and
77 standard deviation of the peak factor [32], [33]. If the process is non-Gaussian, no exact solution exists
78 to predict mean and standard deviation of the peak factors. In general, using a Gaussian approximation
79 yields non-conservative peak factor values when applied to non-Gaussian processes [34].

80 Several analytical models have been proposed in the scientific literature to predict non-Gaussian load
81 effects. Kareem and Zhao [34] proposed an analytical expression for the mean of non-Gaussian peak
82 factors using a moment-based model [31] based on the concept of non-Gaussian translation process [36]
83 with a cubic Hermite polynomial transformation. Winterstein et al. [37] proposed a modification of the
84 Davenport equation for the non-Gaussian peak factor mean by including the effects of clustering. Sadek
85 and Simiu [38] proposed an automated mapping procedure to estimate the peak distribution of wind-
86 induced non-Gaussian internal forces on low-rise buildings by using a database-assisted design software.
87 This mapping procedure requires identifying an analytical marginal probability distribution for the time
88 series of interest through numerical fitting of the distribution parameters. However, the Sadek–Simiu
89 method has been applied only to non-Gaussian processes with an underlying marginal gamma distribution
90 [39], [40], [41], [42], [43].

91 Kwon and Kareem [27] derived an analytical solution for the non-Gaussian peak factor standard deviation
92 based on the Hermite model and proposed a revised Hermite model and a modified Hermite model for
93 estimating the mean and standard deviation of non-Gaussian peak factors. The revised Hermite model is
94 based on the optimal parameters of a four-moment cubic Hermite polynomial transformation [44];
95 however, this model has some validity limitation regarding the specific ranges of the skewness and
96 kurtosis of the process. The modified Hermite model is based on an equivalent statistical cubicization
97 procedure [45], [33] and requires solving of a system of coupled nonlinear equations that depend on the
98 skewness and kurtosis of the process. Huang et al. [42] proposed the Translated-Peak-Process (TPP)

99 model to estimate the local peak distribution, peak factors, and quantiles of peak extremes. The TPP
100 model is a modification of the Sadek-Simiu point-to-point mapping procedure, which assumes a Weibull
101 distribution for the local peaks of non-Gaussian process' time histories. The TPP model was validated by
102 comparing the analytical estimates with wind-tunnel pressure experimental results for a tall building. Ma
103 and Xu [46] proposed a moment-based Johnson transformation method in conjunction with a Gumbel
104 distribution assumption to estimate the statistics of wind pressure peak factors. The results of this method
105 were validated through a comparison with the peak factors obtained from long-duration pressure records
106 measured in wind-tunnel tests on the model surfaces of a high-rise building. It is noted here that, while
107 there is an agreement in the literature that the Davenport model tends to underestimate (sometimes
108 significantly) the mean value of the peak factors, there is no agreement on a single best model for all
109 structures, with different versions of the Hermite model that seem to perform better for roof of low-rise
110 buildings [27], [42], [47], and other approaches that seem to be preferable for the vertical sides of tall
111 buildings [42], [46].

112 Validation of the peak statistics' estimation models available in the literature is extremely limited for
113 HPRs. Ding and Chen [21] compared the accuracy of various methods for extreme value analysis, (i.e.,
114 the peaks-over-threshold method, the average conditional exceedance rate method, and the translation
115 process method with various translation models, including the Hermite model) for select pressure taps'
116 recordings obtained from a wind tunnel test on a saddle-type HPR. Liu et al. [23] investigated different
117 statistics of dynamic pressures on a saddle-type HPR, as well as the dependence of these statistics on
118 different turbulence profiles. They observed that the peak factors in the flow separation regions presented
119 a significant non-Gaussian behavior and that moment-based Hermite estimates were accurate only for
120 mild non-Gaussianity. Liu et al. [24] proposed a new version of the Hermite model, in which modified
121 moments of the original process are used to estimate separately the means of positive and negative peak
122 factors. This model (referred to as the Liu's model hereafter) was verified through a comparison with the

123 peak factors of wind pressures measured in wind tunnel tests on a large-span saddle-type roof. It is
124 noteworthy that the roof considered in [23], [24] is representative only of HPRs with linear edges (i.e.,
125 inclined at 45° with respect to the sagging and hogging directions of the roof). The extreme values of the
126 pressure coefficients on HPRs are significantly affected by turbulence [23] and roof shape [19], [20].
127 However, information on appropriate ranges and/or models for HPRs is lacking in current technical
128 standards and design codes [48], [49], [50], [51], [52], [53], [54], [55], [56]. In addition, there is a need
129 for a detailed comparison of the different analytical models available in the literature in terms of their
130 accuracy in estimating the statistics of wind pressure peak factors for HPRs. It is also noted that, while
131 many studies available in the literature investigate the accuracy of analytical models for individual wind
132 pressure recordings (i.e., single pressure tap and single duration), only few of them investigate the overall
133 accuracy of these models for a given surface, e.g., [42], [46] for the vertical sides of tall buildings, and
134 [47] for the roof of low-rise buildings. Moreover, in these investigations different types of errors have
135 been used to quantify the accuracy of different models, and it is not immediately apparent how the results
136 obtained using different error definitions can be compared. Finally, the authors of the present paper were
137 not able to identify studies that take into consideration the effects of different durations of the wind
138 pressure recordings.

139 Based on an extensive wind-tunnel experimental campaign, the research presented in this paper
140 investigates in detail the statistics of the peak factors in HPRs, as well as the non-Gaussian properties of
141 the peak factors as functions of the position on a square HPR and the relative direction of the wind. This
142 study also investigates the overall relative accuracy of different analytical models for the estimation of
143 peak factor statistics when compared with experimental wind tunnel measurements on a scaled model of
144 a building with a square HPR. This accuracy is investigated for different lengths of the pressure time
145 histories and for different definitions of error.

146 **2 Research relevance**

147 This study provides several new contributions to the field of Structural Wind Engineering. In particular,
148 it provides a better understanding of the Gaussian and non-Gaussian behavior of the local pressure
149 coefficient processes on HPRs, as well as the effect of non-Gaussianity on the peak factor's statistical
150 moments for this structural geometry. This understanding is a necessary step toward the development of
151 modern design guidelines for tensile structures using hyperbolic paraboloid shapes. This study also
152 develops a better understanding of the effects of different time durations with respect to the accuracy of
153 different analytical models for the estimation of the peak factor's statistics. The knowledge of the different
154 models' performance over different time durations allow the identification of which models can be
155 reliably used to extrapolate the peak factor's statistics beyond the time durations that are compatible with
156 specific wind tunnel tests. Finally, to the best of the authors' knowledge, this study presents the first
157 careful comparison of different error measures used to compare the performance of different analytical
158 models. The identification of an appropriate error measure, particularly when considering average errors
159 over an entire surface equipped with numerous pressure taps in wind tunnel tests, can provide important
160 guidance for future experimental and numerical studies to investigate the statistics of pressure coefficients
161 and peak factors for different surface geometries.

162 **3 Description of the model geometry and wind tunnel tests**

163 Wind tunnel testing was carried out in the CRIACIV's open circuit boundary layer wind tunnel in Prato,
164 Italy [19], with a test chamber size 2.3 m x 1.6 m. The test used in this research was performed on a
165 square wood model of HPR with the following geometric parameters: $L_1 = L_2 = 80$ cm = model lengths
166 in the sagging (upward curvature) and hogging (downward curvature) directions, respectively
167 (corresponding to the cable spans of the roof); $f_1 = 2.67$ cm = model sag in the sagging direction; $f_2 = 5.33$
168 cm = model sag in the hogging direction; $H_1 = 13.33$ cm = height of the lowest roof point in the sagging
169 direction; and $H_2 = 21.33$ cm = height of the highest roof point in the hogging direction (Figure 1). It is

170 observed that this model is different from that considered in [23], [24], because it has curved edges instead
171 of linear edges, i.e., the sides of the square plan coincide with the roof's sagging and hogging directions.
172 The wind directions considered in the wind tunnel tests are indicated in Figure 1. The direction
173 corresponding to a wind angle of attack $\theta = 0^\circ$ is parallel to the hogging direction, whereas the direction
174 corresponding to $\theta = 90^\circ$ is parallel to the sagging direction of the roof.

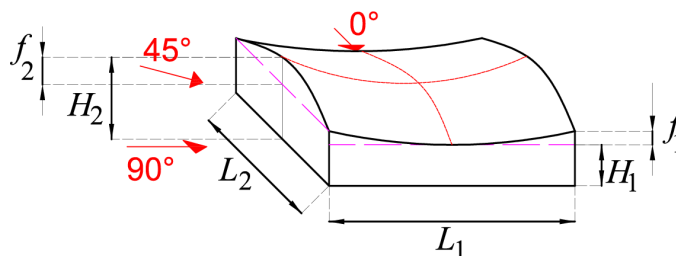


Figure 1. Geometry of the hyperbolic paraboloid model.

175 A picture of the rigid wood model tested in the wind tunnel is shown in Figure 2. The wood model was
176 fitted with 181 pressure taps on the lateral surfaces and 89 pressure taps on the roof. All pressure taps
177 were connected to pressure scanners through polytetrafluoroethylene tubes, calibrated to obtain a flat
178 frequency response in the range of interest (from 0 to 100 Hz).

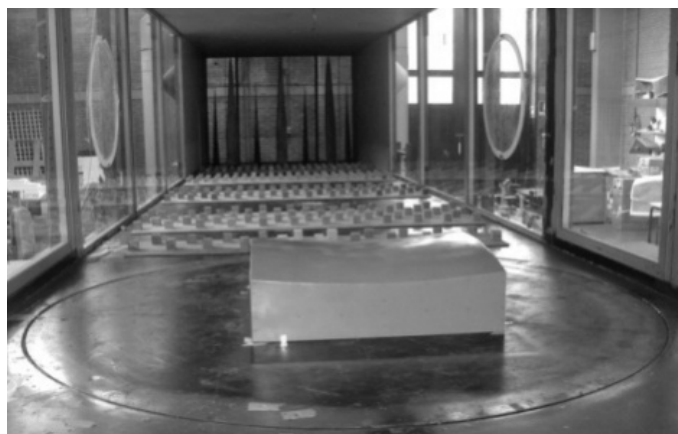
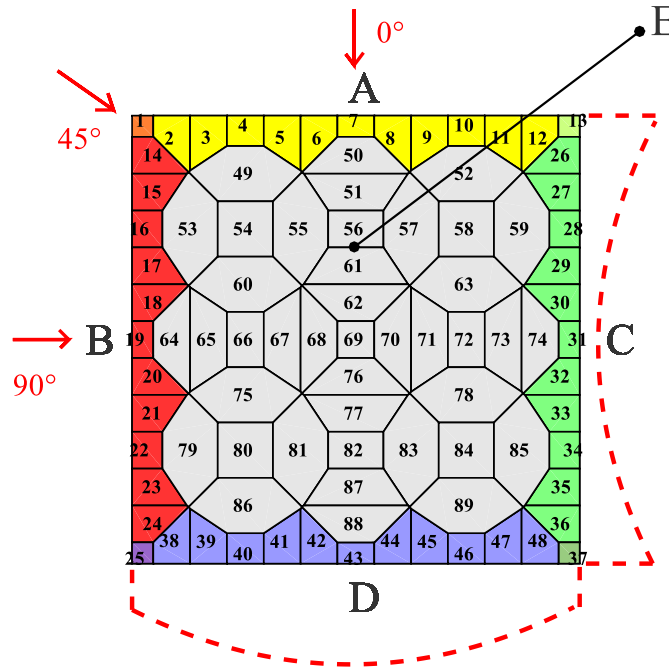


Figure 2. In-scale wind tunnel physical model.

179 The roof pressure taps were distributed according to the map shown in Figure 3, which also shows five
180 different significant roof portions, referred to as zone A through zone E. Zone A is the edge detachment
181 zone for $\theta = 0^\circ$, zone B is the edge detachment zone for $\theta = 90^\circ$, zone C represents the roof edge parallel
182 to zone B, zone D represents the roof edge parallel to zone A, and zone E corresponds to the central

183 portion of the roof. The wind tunnel tests were performed with an average wind speed of 16.7 m/s at a
 184 height of 10 cm, a sampling frequency equal to 252 Hz and an acquisition time $T_0 = 30$ s. The recording
 185 duration corresponds to an equivalent-time duration of approximately 30 minutes when considering a
 186 scale 1/100 for the physical model with respect to a full-scale structure. Additional information on the
 187 test setup and results can be found in [19], where the average pressure coefficients on the roof and walls
 188 were presented for several geometrical models of HPRs. The experimental results of relevance for the
 189 present study are reported in the following section of this paper.



190 Figure 3. Pressure taps' location and zone identification on the HPR.

191 4 Experimental results

192 Figure 5 through Figure 7 report relevant statistics of the wind tunnel experimental results for $\theta = 0^\circ$, 45° ,
 193 and 90° , respectively, based on the experimental campaign described in [19], [22], calculated over the
 194 entire duration of the recorded time-histories, i.e., for $T_0 = 30$ s, by assuming that the underlying process
 195 is stationary. In particular, the different subfigures present the mapping for all pressure taps of the
 196 following pressure coefficient's statistics: (a) mean, μ_{c_p} (previously reported in Rizzo et al. (2011) [19]

197 but repeated here for the sake of completeness); (b) standard deviation, σ_{c_p} ; (c) skewness coefficient, γ_{c_p} ;
 198 (d) excess kurtosis, κ_{c_p} ; (e) mean zero-crossing rate, ν_0 (obtained as the average between the total up-
 199 crossings and down-crossings of the zero level divided by the record duration, e.g., see [21], [57]); and
 200 (f) peak factor, g_{T_0} . Standard deviation, skewness coefficient, and excess kurtosis are scaled up by a factor
 201 equal to 10 for the sake of presentation clarity.

202 In this study, positive values of the pressure coefficients correspond to suction (i.e., to a pressure lower
 203 than the static pressure of the undisturbed wind flow, p_0). Thus, the time variant pressure coefficient at
 204 the i -th pressure tap ($i = 1, \dots, 89$) is given by:

$$c_{p,i}(t) = \frac{p_0 - p_i(t)}{\frac{1}{2}\rho \cdot V_m^2} \quad (1)$$

205 where $p_i(t)$ denotes the wind pressure measured at time t for pressure tap i on the roof surface, ρ denotes
 206 the air density, and V_m denotes the mean speed of the undisturbed wind flow. It is noted here that higher-
 207 order statistical moments (i.e., skewness and excess kurtosis) have higher variability than lower-order
 208 statistical moments (i.e., mean and standard deviation), particularly for non-Gaussian processes [58]. This
 209 phenomenon is related to the need to achieve approximate stationarity of the underlying process in order
 210 to obtain reliable estimates of the statistical moments. In order to identify potential inaccuracies in the
 211 estimates of higher-order moments, the variability of these statistical moments was investigated as a
 212 function of the duration of the time interval over which they were estimated. For all pressure taps and all
 213 directions considered in this investigation, it was found that in almost all cases: (1) the pressure
 214 coefficient's means and standard deviations converged before 5 s of recorded time histories, (2) the
 215 pressure coefficient's skewness converged before 22 s of recorded time histories, and (3) the pressure
 216 coefficient's excess kurtosis converged before 27 s of recorded time histories. Figure 4 shows the values
 217 of the pressure coefficient's mean, standard deviation, skewness, and excess kurtosis as functions of the
 218 experimental record's time duration for two representative pressure taps (i.e., pressure taps 11 and 5 for

219 wind angles $\theta = 0^\circ$ and 90° , respectively). Based on these results, it is concluded that the values of the
220 pressure coefficient's statistical moments (in particular, skewness and excess kurtosis) correspond to the
221 converged constant values for the underlying stationary processes.

222 It is observed that the mean pressure coefficients assume positive values at all locations for all three wind
223 angles of attack, i.e., the wind action on the roof overall correspond to a suction force. However, for a
224 few pressure taps, negative values of the pressure coefficients (i.e., pressures that are higher than p_0) were
225 recorded for short portions of the time histories. With the exceptions of mean and standard deviations of
226 the pressure coefficients, all calculations were performed after the signals were subtracted from their
227 corresponding mean values and normalized by their corresponding standard deviations (to obtain a zero-
228 mean process with unit standard deviation, see, e.g., [27]). The experimental results are presented in the
229 following subsections for each of the considered wind angles of attack.

230 ***4.1 Statistics of pressure coefficients for wind angle of attack $\theta = 0^\circ$***

231 For $\theta = 0^\circ$, the mean pressure coefficients vary significantly with the location of the pressure tap, with
232 values ranging from 1.332 to 0.192 (Figure 5a). The values of the mean pressure coefficients are highest
233 along the edge detachment zone A, after which they drop immediately to low values, slightly increase
234 toward the middle of the roof and then decrease again to the lowest values in zone D. The standard
235 deviations of the pressure coefficients assume their highest values in zone A with the maximum value
236 equal to 0.367, their intermediate values in zones B and C, and their lowest values in zones D and E, with
237 the minimum value equal to 0.040 (Figure 5b).

238

239

240

241

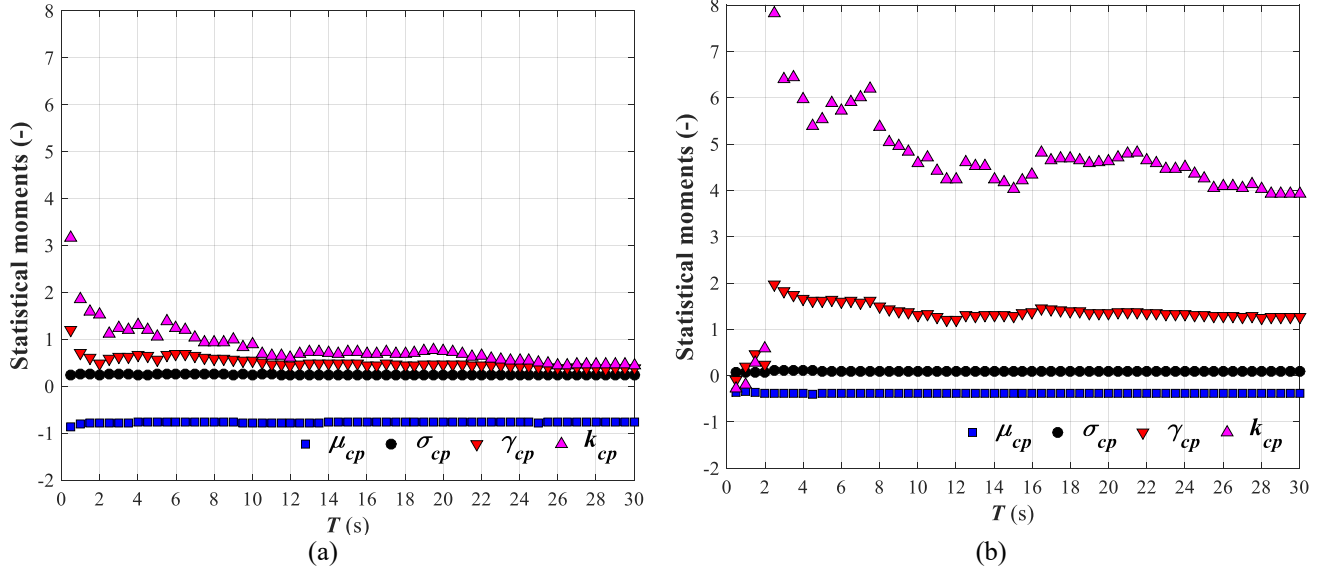
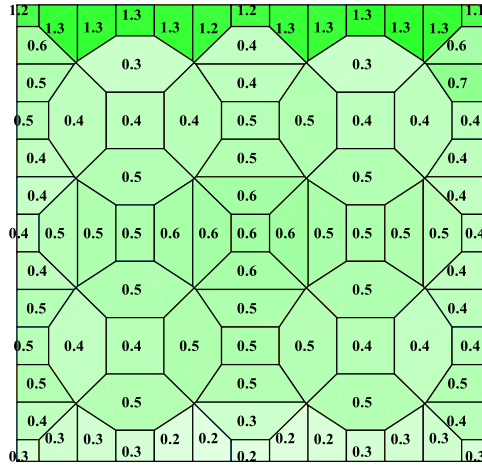


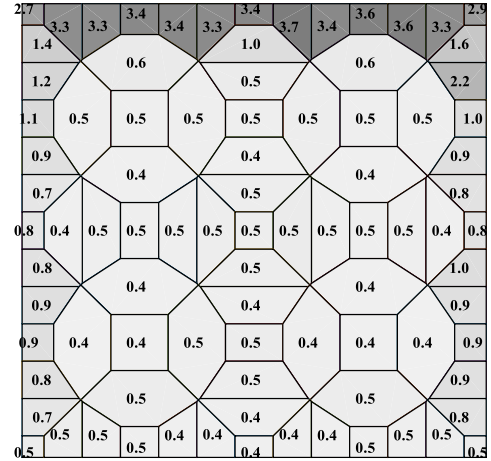
Figure 4. Values of the pressure coefficient's mean, standard deviation, skewness, and excess kurtosis as functions of the experimental record's time duration: (a) pressure tap #11 for $\theta = 0^\circ$, and (b) pressure tap #5 for $\theta = 90^\circ$.

242 The skewness coefficient (Figure 5c) and excess kurtosis (Figure 5d) exhibit a very similar trend, i.e.,
 243 they are generally highly correlated. In fact, they assume their highest positive values toward the middle
 244 of zones B and C (1.486 for the skewness coefficient and 7.236 for the excess kurtosis, respectively),
 245 intermediate positive values in the remainder of zones B and C as well as in zone A, and low magnitude
 246 positive or negative values in zones D and E (with the minimum values equal to -0.098 for the skewness
 247 coefficient and -0.374 for the excess kurtosis, respectively). According to [58], the roof regions where
 248 the pressure coefficient process is non-Gaussian are identified by $|\gamma_{cp}| > 0.5$ and/or $|k_{cp}| > 0.5$. Based
 249 on this criterion and the results reported in Figure 5c and Figure 5d, the considered process is non-
 250 Gaussian in most of the pressure taps located in zones A, B, and C.
 251 The mean zero-crossing rate presents a smaller variability than other statistics, with the maximum and
 252 minimum values equal to 15.989 Hz and 8.364 Hz, respectively (Figure 5e). The largest values for ν_0 are
 253 observed in zones A, B, and C. The peak factors show a trend similar to that of the mean zero-crossing
 254 rate. In this case, the largest values for the peak factors (i.e. the maximum is equal to 10.298) are observed
 255 near the middle of zones B and C, i.e., near the highest portions of the roof (Figure 5f), which correspond
 256 also to the zones with the largest values of the skewness coefficient and excess kurtosis. Relatively large

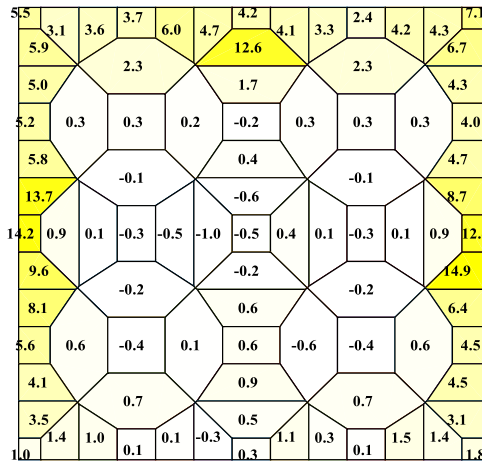
257 values of the peak factors (in the range 4.0 to 6.5) are observed in the remainders of zones B and C, in
258 zone A and in the portion of zone E immediately near to zone A. The peak factors assume values close to
259 3.5 in most of zone E and in zone D, i.e., in the roof region where the process describing the pressure
260 coefficient can be considered Gaussian. It is noteworthy that a value of 3.4 to 3.5 for the peak factor is
261 often used in design applications [52], based on the assumption that the underlying process is Gaussian.
262 The observed maximum and minimum values of the peak factor are equal to 10.298 and 2.987,
263 respectively.



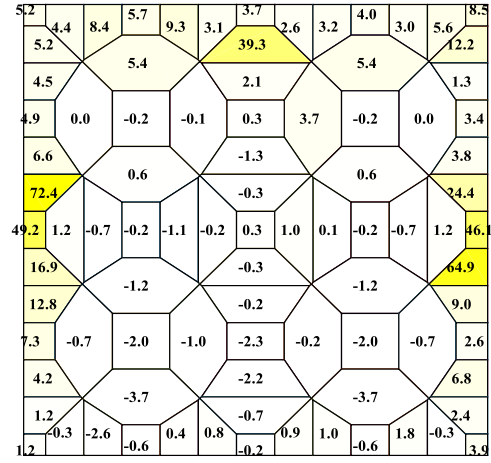
(a)



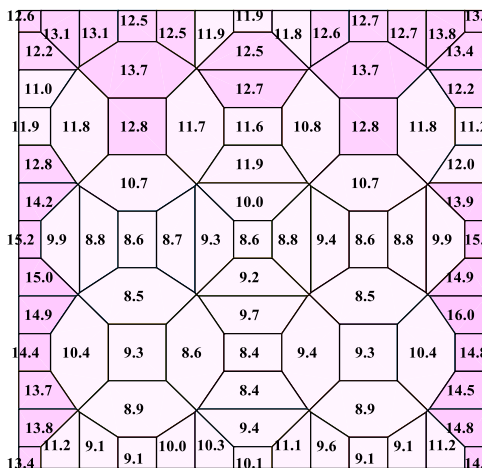
(b)



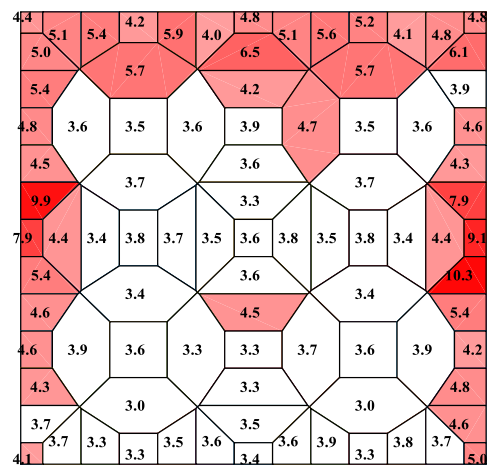
(c)



(d)



(e)



(f)

Figure 5. Statistics of wind pressure coefficients for $\theta = 0^\circ$: (a) mean, μ_{c_p} ; (b) standard deviation (scaled up by 10), σ_{c_p} ; (c) skewness coefficient (scaled up by 10), γ_{c_p} ; (d) excess kurtosis (scaled up by 10), κ_{c_p} ; (e) mean zero-crossing rate, ν_0 (Hz); and (f) peak factor, g_{T_0} .

265 As expected from the geometry of the roof and the wind flow, the trends for all the considered statistics
266 are almost symmetric with respect to the centerline of the roof that is parallel to the hogging direction. It
267 is also observed that non-Gaussianity appears to be not necessarily correlated with the magnitude of the
268 pressure coefficients' mean and standard deviation.

269 *4.2 Statistics of pressure coefficients for wind angle of attack $\theta = 45^\circ$*

270 For $\theta = 45^\circ$, the mean pressure coefficients are slightly higher than those for $\theta = 0^\circ$ and vary between
271 1.607 and 0.161 (Figure 6a). The highest values of the mean pressure coefficients are observed near the
272 detachment zone along the hogging direction (zone B and part of zone E). The maximum value is reached
273 at the highest point of the roof in zone B. Zone A contains the intermediate values of the mean pressure
274 coefficients, whereas zones C, D, and E have smaller values.

275 The standard deviations of the pressure coefficients assume their highest values also in zone B and part
276 of zone E, with the maximum value equal to 0.491 observed at pressure tap #64, i.e., in zone E next to
277 the pressure tap located at the highest point of the roof (Figure 6b). The standard deviations of the pressure
278 coefficients assume intermediate values in zone A and smaller values in the remainder of the roof, with
279 the minimum value equal to 0.035.

280 The skewness coefficient assumes its highest values near the lowest point of the roof from the side of
281 attack for the wind, i.e., toward the middle of zone A and the neighboring portion of zone E, as well as at
282 the far corner of zone B (Figure 6c). The maximum value is equal to 1.299 and is observed at pressure
283 tap #50. Several pressure taps in zone D and E have negative skewness coefficients, with values as low
284 as -0.529. The excess kurtosis assumes large values in zone B with the exclusion of the corners and in the
285 middle of zones A and (in minor measure) D (Figure 6d). The maximum value is 4.744 and is observed
286 at pressure tap #27. Lower values are generally observed in zone D, where negative values are measured
287 at a few pressure taps. However, the lowest value of -0.601 is achieved at pressure tap #64, in zone E next
288 to zone B. It is also observed that a significant portion of the pressure taps of the roof have excess kurtosis

289 values larger than 0.50, which is the conventional value suggested in [58] above which the pressure
290 coefficient process can be considered non-Gaussian.

291 The mean zero-crossing rate presents larger values around the edges defined by zones A, B, and C, with
292 values as high as 18.038 Hz, and smaller values elsewhere, with values as low as 10.278 Hz (Figure 6e).

293 The peak factors assume values higher than 4.0 in most of the pressure taps, with the highest values
294 observed in zone C and the maximum value equal to 10.570 achieved at pressure tap #27 (Figure 6f). The
295 minimum value of the peak factor is equal to 3.319 and is measured at pressure tap #64 in zone E. For
296 this wind angle of attack, the relatively high values of the peak factors seem to confirm the previous
297 observation, based only on the values of skewness coefficient and excess kurtosis, that the pressure
298 coefficient process is non-Gaussian on most of the roof.

299 **4.3 Statistics of pressure coefficients for wind angle of attack $\theta = 90^\circ$**

300 For $\theta = 90^\circ$, the mean pressure coefficients are lower than for $\theta = 45^\circ$ and have a slightly higher variability
301 than those for $\theta = 0^\circ$. The highest values are achieved in zone B, with the maximum value equal to 1.426
302 at pressure tap #1 (i.e., at the corner near zone A, see Figure 7a). The mean pressure coefficients decrease
303 slowly moving from zone B through zone E, where the minimum value of 0.090 is achieved, and then
304 increase again in zone C. The standard deviations of the pressure coefficients follow a trend similar to
305 that of the mean pressure coefficients (Figure 7b). In fact, they assume their largest values overall in zone
306 B, even though the maximum value equal to 0.397 is observed in pressure tap #64 (i.e. zone E). The
307 standard deviations then gradually decrease moving from the detachment edge to the other side of the
308 roof, with the lowest values overall in zone E.

309

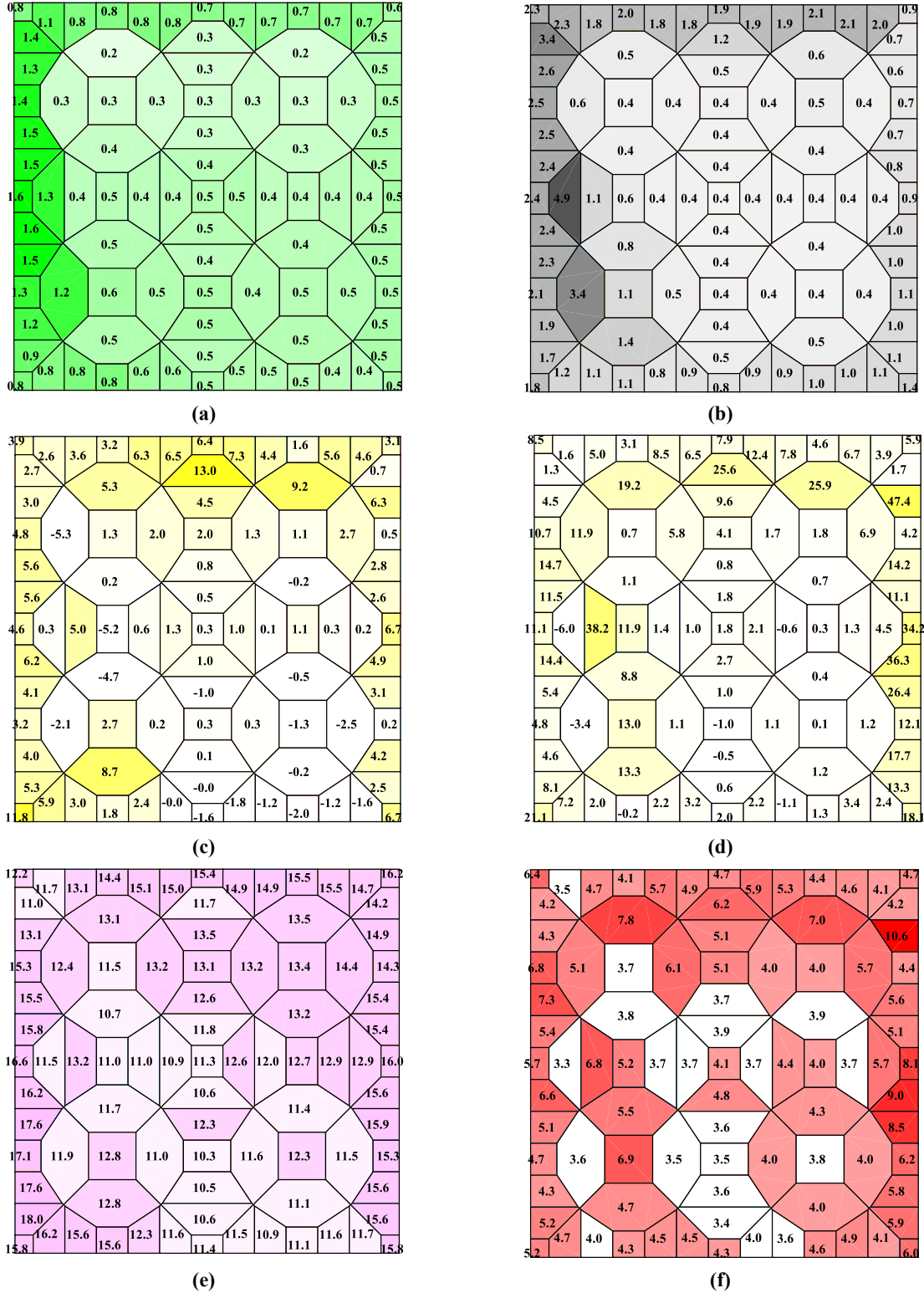


Figure 6. Statistics of wind pressure coefficients for $\theta = 45^\circ$: (a) mean, μ_{c_p} ; (b) standard deviation (scaled up by 10), σ_{c_p} ; (c) skewness coefficient (scaled up by 10), γ_{c_p} ; (d) excess kurtosis (scaled up by 10), κ_{c_p} ; (e) mean zero-crossing rate, ν_0 (Hz); and (f) peak factor, g_{T_0} .

310 The skewness coefficient assumes its highest positive values near the detachment edge in zone B, with
311 the maximum value equal to 1.454 at pressure tap #15 and all values above the Gaussianity threshold of
312 0.5 (Figure 7c). The skewness coefficient assumes intermediate positive values, only few of which are
313 above the Gaussianity threshold of 0.5, along the two edges that are parallel to the wind flow (i.e., zones
314 A and D). It reaches the lowest values in zones C and E, with the minimum equal to -0.249 at pressure
315 tap #83. It is also observed that, in zones C and E, the skewness coefficient is negative only at a few of
316 the pressure taps and is higher in absolute value than the Gaussianity threshold of 0.5 only at two pressure
317 taps. The excess kurtosis follows a trend similar to that of the skewness coefficient, with the highest
318 values in zone B and the maximum value of 5.345 at pressure tap #15, intermediate values in zones A
319 and D, and lowest values in zones C and E (Figure 7d). The minimum value is equal to -0.143 and is
320 reached at pressure tap #27. Only three pressure taps, all located in zone C, have negative values of excess
321 kurtosis. More than half of the pressure taps present an excess kurtosis higher in absolute value than the
322 Gaussianity threshold of 0.5, i.e., in most of the roof the pressure coefficient process can be considered
323 non-Gaussian.

324 The mean zero-crossing rate presents larger values in zones A, D, and E and lower values at the two edges
325 orthogonal to the wind flow (Figure 7e), with the maximum value equal to 16.997 Hz and the minimum
326 value equal to 8.632 Hz. The peak factors assume values higher than 4.0 in almost all the pressure taps,
327 with the exception of 13 pressure taps, of which eight are located in zone C and 5 in zone E (Figure 7f).
328 The highest values are reached along the detachment edge in zone B, where the maximum value is equal
329 to 9.093 at pressure tap #19 (i.e., at the highest point of the roof), and along the two sides parallel to the
330 wind flow (i.e., zones A and D). The minimum value is equal to 3.573 and is achieved at pressure tap #27
331 in zone C. For this wind angle of attack, the overall high values of the peak factors are consistent with the
332 high values of skewness coefficient and excess kurtosis and indicate that the pressure coefficient process
333 is non-Gaussian on most of the roof.

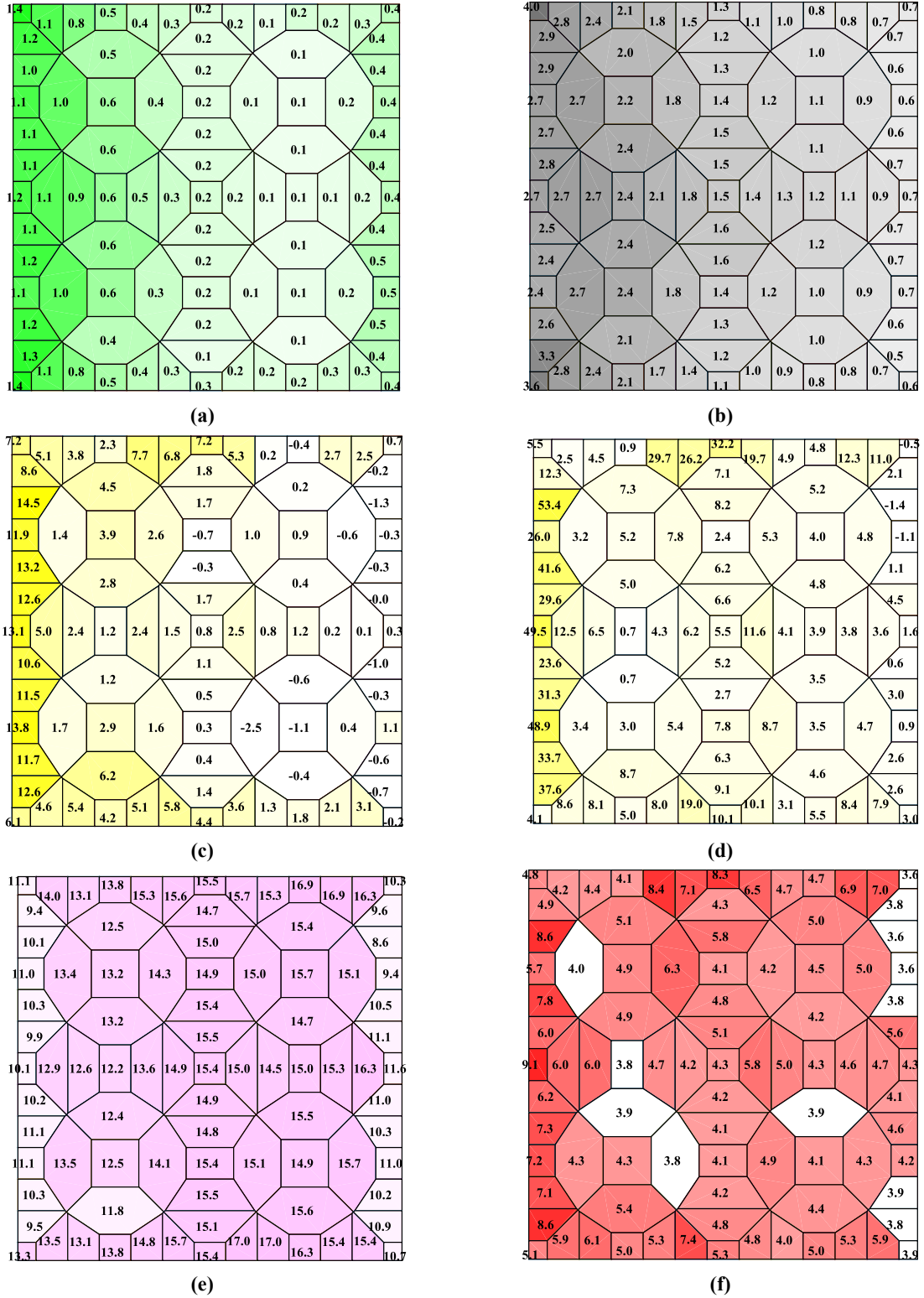


Figure 7. Statistics of wind pressure coefficients for $\theta = 90^\circ$: (a) mean, μ_{c_p} ; (b) standard deviation (scaled up by 10), σ_{c_p} ; (c) skewness coefficient (scaled up by 10), γ_{c_p} ; (d) excess kurtosis (scaled up by 10), κ_{c_p} ; (e) mean zero-crossing rate, ν_0 (Hz); and (f) peak factor, g_{T_0} .

334 5 Analytical estimates of peak factor statistics

335 This section briefly describes six different analytical models for the statistics of the peak factor, which
336 have been proposed in the literature, namely the Davenport, classical Hermite, revised Hermite, modified
337 Hermite, TPP, and Liu's models. The peak factor statistics considered in this study are: (1) the mean
338 value, $\mu_{g,M}(T)$; (2) the standard deviation, $\sigma_{g,M}(T)$; and (3) the α -quantile, $X_{g,M}^\alpha(T)$; in which α denotes
339 the quantile rank, i.e., $\alpha = P[g_T \leq X_{g,M}^\alpha(T)]$, where $P[\dots]$ denotes the probability of the event defined
340 in the square brackets; $M = D$ (for Davenport model), H (for classical Hermite model), rH (for revised
341 Hermite model), mH (for modified Hermite model), TPP (for TPP model), or L (for Liu's model); and T
342 denotes the time interval of reference.

343 5.1 Davenport model

344 The Davenport peak factor statistics are based on the assumption that the underlying process is Gaussian
345 [32]. The distribution of the local peaks (i.e., local maxima in time) of a standardized Gaussian process
346 reduces to the Rayleigh distribution for narrow-band processes [60]. Davenport peak factor is often
347 employed in wind engineering practice [52] to estimate the mean extreme value (i.e., the mean value of
348 the global maximum in time) of wind-induced responses. The statistics of the Davenport peak factor are
349 given by [32]:

$$\mu_{g,D}(T) = \beta + \frac{\gamma}{\beta} \quad (2)$$

$$\sigma_{g,D}(T) = \frac{\pi}{\beta\sqrt{6}} \quad (3)$$

$$X_{g,D}^\alpha(T) = \sqrt{2 \ln(v_0 \cdot T) - 2 \ln(-\ln \alpha)} \quad (4)$$

350 in which $\gamma \approx 0.5772$ is the Euler's constant, and $\beta = \sqrt{2 \ln(v_0 \cdot T)}$. Eq. (4) is derived here directly from
351 the distribution of the largest peak value presented in [32].

352 **5.2 Hermite models**

353 The classical, revised, and modified Hermite models belong to the same family of analytical models based
 354 on a translation model using a third-order Hermite polynomial. The analytical expression of the classical
 355 Hermite model's mean peak factor was proposed in [34] to account for non-Gaussianity of wind
 356 processes. The model was further extended to provide an analytical estimate of the standard deviation of
 357 the peak factor in [27]. In order to estimate the quantiles, it is assumed here that the distribution of the
 358 largest peak values is a Gumbel distribution, which implies a Weibull distribution for the local peaks of
 359 the pressure coefficients, as suggested in [42].

$$\mu_{g,H}(T) = k \cdot \left\{ \begin{array}{l} \left(\beta + \frac{\gamma}{\beta} \right) + h_3 \cdot \left(\beta^2 + 2\gamma - 1 + \frac{1.98}{\beta^2} \right) \\ + h_4 \cdot \left[\beta^3 + 3\beta(\gamma - 1) + \frac{3}{\beta} \cdot \left(\frac{\pi^2}{6} - \gamma + \gamma^2 \right) + \frac{5.44}{\beta^3} \right] \end{array} \right\} \quad (5)$$

$$\sigma_{g,H}(T) = k \cdot \left[\begin{array}{l} \frac{\pi^2}{6\beta^2} + 6.58h_3^2 + 9h_4^2 \cdot \left(1.64\beta^2 + \frac{12.69}{\beta^2} + 5.32 \right) + 6.58 \frac{h_3}{\beta} \\ + 6h_4 \cdot \left(\frac{2.66}{\beta^2} + 1.64 \right) + 12h_3h_4 \cdot \left(1.64\beta + \frac{2.66}{\beta} \right) \end{array} \right]^{\frac{1}{2}} \quad (6)$$

$$X_{g,H}^\alpha(T) = \mu_{g,H}(T) - \frac{\sqrt{6}}{\pi} \cdot [\gamma + \ln(-\ln \alpha)] \cdot \sigma_{g,H}(T) \quad (7)$$

360 in which

$$h_3 = \frac{\gamma_{c_p}}{4 + 2\sqrt{1 + 1.5\kappa_{c_p}}}, h_4 = \frac{\sqrt{1 + 1.5\kappa_{c_p}} - 1}{18}, k = \frac{1}{\sqrt{1 + 2h_3^2 + 6h_4^2}} \quad (8)$$

361 For Gaussian processes, $\gamma_{c_p} = \kappa_{c_p} = h_3 = h_4 = 0$ and $k = 1$; thus Eqs. (5) and (6) reduce to Eqs. (2)
 362 and (3), respectively.

363 The revised Hermite model is a modification of the classical Hermite model, in which the expressions for
 364 parameters h_3 and h_4 given in Eq. (8) are substituted by the values \hat{h}_3 and \hat{h}_4 that minimize the lack-of-
 365 fit errors in skewness and kurtosis of the Hermite model [37], [44], which are given by:

$$\hat{h}_3 = \frac{\gamma_{c_p}}{6} \cdot \left[\frac{1 - 0.015 |\gamma_{c_p}| + 0.3\gamma_{c_p}^2}{1 + 0.2\kappa_{c_p}} \right] \quad (9)$$

$$\hat{h}_4 = \left[\frac{\left(1 + 1.25\kappa_{c_p}\right)^{\frac{1}{3}} - 1}{10} \right] \cdot \left[1 - \frac{1.43\gamma_{c_p}^2}{\kappa_{c_p}} \right]^{(1-0.1\kappa_{c_p}^{0.8})} \quad (10)$$

366 The analytical solutions for the mean, $\mu_{g,rH}(T)$, and standard deviation, $\sigma_{g,rH}(T)$, of the peak factor using
 367 the revised Hermite model are given by Eqs. (5) and (6), respectively, by substituting h_3 with \hat{h}_3 and h_4
 368 with \hat{h}_4 , respectively. The expression for the quantile of the revised Hermite model, $X_{g,rH}^\alpha(T)$, is given by
 369 Eq. (7) by substituting $\mu_{g,H}(T)$ with $\mu_{g,rH}(T)$ and $\sigma_{g,H}(T)$ with $\sigma_{g,rH}(T)$, respectively. It is noteworthy
 370 that the revised Hermite model is valid only for the ranges $0 < \gamma_{c_p} < 12$ and $0 \leq \kappa_{c_p}^2 < 2\gamma_{c_p}/3$. In the
 371 case in which these conditions on skewness coefficient and excess kurtosis are not satisfied, the revised
 372 Hermite model reverts to the classical Hermite model.

373 The modified Hermite model [45], [61] is a modification of the classical Hermite model, in which the
 374 shape parameters \hat{c}_3 and \hat{c}_4 that define the third-order Hermite polynomial of the translation model are
 375 related to γ_{c_p} and κ_{c_p} by

$$\gamma_{c_p} = k^3 \cdot (8\hat{c}_3^3 + 108\hat{c}_3 \cdot \hat{c}_4^2 + 36\hat{c}_3 \cdot \hat{c}_4 + 6\hat{c}_3) \quad (11)$$

$$\kappa_{c_p} + 3 = k^4 \cdot \left(\begin{array}{l} 60\hat{c}_3^4 + 3348\hat{c}_4^4 + 2232\hat{c}_3^2 \cdot \hat{c}_4^2 + 60\hat{c}_3^2 + 252\hat{c}_4^2 \\ + 1296\hat{c}_4^3 + 576\hat{c}_3^2 \cdot \hat{c}_4 + 24\hat{c}_4 + 3 \end{array} \right) \quad (12)$$

376 Eqs. (11) and (12) cannot be inverted analytically and need to be solved numerically; however Yang et
 377 al. [61] presented an approximate polynomial solution for \hat{c}_3 and \hat{c}_4 as functions of to γ_{c_p} and κ_{c_p} . The
 378 analytical solutions for the mean, $\mu_{g,mH}(T)$, and standard deviation, $\sigma_{g,mH}(T)$, of the peak factor
 379 corresponding to the modified Hermite model are given by Eqs. (5) and (6), respectively, by substituting
 380 h_3 with \hat{c}_3 and h_4 with \hat{c}_4 , respectively. Similar to the case of the revised Hermite model, the expression

381 for the quantile of the modified Hermite model, $X_{g,rH}^\alpha(T)$, is given by Eq. (7) by substituting $\mu_{g,H}(T)$ with
382 $\mu_{g,mH}(T)$ and $\sigma_{g,H}(T)$ with $\sigma_{g,mH}(T)$, respectively. The region of applicability of the modified Hermite
383 model is defined by $\hat{c}_3^2 + 3\hat{c}_4 \cdot (3\hat{c}_4 - 1) < 0$ [41], which can be approximated in terms of skewness
384 coefficient and excess kurtosis as $-\gamma_{c_p} + (1.25\kappa_{c_p})^2 \leq 0$ [62]. If these conditions on \hat{c}_3 and \hat{c}_4 or on γ_{c_p}
385 and κ_{c_p} are not satisfied, the modified Hermite model reverts to the classical Hermite model.

386 **5.3 Translated-Peak-Process (TPP) model**

387 The TPP model assumes that the pressure coefficient's local peaks follow a Weibull distribution and,
388 thus, that the distribution of the largest peak value is a Gumbel distribution [42]. The TPP model uses a
389 point-to-point mapping between the cumulative distribution function (CDF) of the local peaks for a
390 Gaussian process, which corresponds to a Rayleigh distribution, and the CDF of the local peaks of the
391 considered non-Gaussian process, which corresponds to the assumed Weibull distribution. This mapping
392 procedure is used to estimate the scale and shape parameters, ρ and κ , respectively, of the underlying
393 Weibull distribution, knowing which the statistics of the peak factor can be determined in closed-form as
394 follows:

$$\mu_{g,TPP}(T) = [\rho \cdot \ln(v_0 \cdot T)]^{\frac{1}{\kappa}} + \frac{\gamma \cdot \left[\rho \cdot \ln(v_0 \cdot T) \right]^{\frac{1}{\kappa}}}{\kappa \cdot \ln(v_0 \cdot T)} \quad (13)$$

$$\sigma_{g,TPP}(T) = \frac{\pi}{\sqrt{6}} \frac{[\rho \cdot \ln(v_0 \cdot T)]^{\frac{1}{\kappa}}}{\kappa \cdot \ln(v_0 \cdot T)} \quad (14)$$

$$X_{g,TPP}^\alpha(T) = [\rho \cdot \ln(v_0 \cdot T)]^{\frac{1}{\kappa}} - \frac{[\rho \cdot \ln(v_0 \cdot T)]^{\frac{1}{\kappa}}}{\kappa \cdot \ln(v_0 \cdot T)} \cdot \ln(-\ln\alpha) \quad (15)$$

395 **5.4 Liu's model**

396 Liu et al. [24] derived a new moment-based translation model by defining a modified probability density
397 function (PDF) that is symmetric around the median of the original non-Gaussian process. By ordering

398 the experimental data at different instants of time in increasing values x_i ($i = 1, \dots, m, m + 1, \dots, N$),
 399 where N is the total number of recorded values and $i \geq m$ corresponds to values $x_i > m_x$, in which m_x
 400 denotes the median of the recorded values, the first four statistical moments of the modified PDF are
 401 obtained as follows:

$$\mu_1 = m_x \quad (16)$$

$$\mu_2 = \left[\left(\frac{2}{N-1} \right) \cdot \sum_{i=m}^N (x_i - \mu_1)^2 \right]^{\frac{1}{2}} \quad (17)$$

$$\mu_3 = 0 \quad (18)$$

$$\mu_4 = \left(\frac{2}{N-1} \right) \cdot \sum_{i=m}^N \left(\frac{x_i - \mu_1}{\mu_2} \right)^4 \quad (19)$$

402 Using this new PDF, the parameters $\mu_{g,\text{new}}(T)$ and $\sigma_{g,\text{new}}(T)$ are calculated using Eqs. (5) and (6),
 403 respectively, with h_3 , h_4 and k given by Eq. (8), where γ_{c_p} and κ_{c_p} are substituted with μ_3 and $\mu_4 - 3$,
 404 respectively. Finally, the peak factor mean and standard deviation can be obtained as:

$$\mu_{g,L}(T) = \frac{1}{\sigma_{c_p}} \cdot \left(\mu_2 \cdot \mu_{g,\text{new}}(T) + \mu_1 - \mu_{c_p} \right) \quad (20)$$

$$\sigma_{g,L}(T) = \frac{\mu_2}{\sigma_{c_p}} \cdot \sigma_{g,\text{new}}(T) \quad (21)$$

405 It is noted here that Eqs. (17) and (19) are different from those given in the original paper [24], which
 406 contain a typographical error; and that Eqs. (20) and (21) were newly derived in order to allow for a direct
 407 comparison of peak factor means and standard deviations obtained from different models.

408 **6 Comparison of experimental and analytical peak factor statistics**

409 This section presents a comparison between experimentally measured and analytically estimated statistics
 410 of the peak factor for the square HPR considered in this study. First, a comparison of the different
 411 analytical models is made by evaluating the percentages of experimental peak factors that have smaller

412 values than different analytical quantiles for an interval of time $T = T_0$ (i.e., for the entire duration of the
413 recorded signals) at different locations on the roof. Second, the different analytical models are compared
414 in terms of estimates of the mean and standard deviation of the peak factors for shorter time intervals.
415 Different error measures are considered and the implications of using these different error measures are
416 discussed. The goal of this section is to identify advantages and limitations of the different analytical
417 models for estimating peak factors for HPRs with respect to location on the roof, wind direction relative
418 to the roof, and duration of the signal. All results are presented only for the Davenport, modified Hermite,
419 TPP, and Liu's models out of the six models described before, i.e., due to space constraints, only the
420 results corresponding to the modified Hermite model are presented among those of the Hermite models.
421 This selection was made because the three Hermite models provided very similar results in all cases and
422 the modified Hermite model was consistently the most accurate of the three Hermite models considered
423 here when compared to the experimental peak factors.

424 **6.1 Comparison of peak factor statistics for $T = T_0$**

425 The comparison of the experimental and analytical peak factor statistics for $T = T_0 = 30$ s
426 (corresponding approximately to a duration of 30 min in full-scale) is performed first for the three wind
427 angles of attack one at the time, after which some synoptic considerations are provided.

428 **6.1.1 Wind angle of attack $\theta = 0^\circ$**

429 Figure 8 shows the analytical estimates of the peak factor mean for a time interval $T = T_0$ and wind angle
430 $\theta = 0^\circ$. These analytical results can be directly compared to the experimental results for the peak factor
431 g_{T_0} reported in Figure 5f.

432 The results reported in Figure 8a show that the Davenport estimate of the peak factor mean changes very
433 little with the location of the pressure tap, with slightly higher values at the highest point of the roof along
434 the edges parallel to the wind flow (i.e., in zones B and C). The maximum and minimum values are equal

435 to 3.653 and 3.470, respectively. By comparing Figure 8a and Figure 5f, it is observed that the Davenport
436 peak factor means significantly underestimate the experimental peak factors in zones A, B, and C, and
437 fail to capture the large peak factor values at the highest points of the roof in zones B and C.

438 The analytical estimates of the peak factor mean for the modified Hermite models are presented in Figure
439 8b. The results of the modified Hermite model are able to reproduce the large values of the experimental
440 peak factors that were observed in the regions where the pressure coefficient process is non-Gaussian,
441 i.e., in zones A, B, and C. The maximum value of the peak factor mean is equal to 8.750; the minimum
442 value of the peak factor mean is equal to 3.014.

443 The TPP estimates of the peak factor mean are shown in Figure 8c. The peak factor means have a trend
444 similar to those of the experimental values, with higher values in zones A, B, and C, and the highest
445 values near the highest points of the roof in zones B and C. The maximum and minimum values of the
446 peak factor mean are equal to 6.840 and 3.292, respectively. It is observed that, even though the TPP
447 model is able to identify the regions of non-Gaussianity that are characterized by higher values of the
448 peak factor, it often underestimates the non-Gaussian peak factors, sometimes even significantly.

449 The Liu's model estimates of the peak factor mean are shown in Figure 8d. These analytical results present
450 a good agreement with the experimental peak factors shown in Figure 5f. Similar to the modified Hermite
451 and TPP models, the highest values are obtained in zones A, B, and C. The maximum and minimum
452 values of the peak factor mean are equal to 9.948 and 2.787, respectively. In the non-Gaussian regions, it
453 is observed that these results are very close to those obtained using the modified Hermite model.

454 It is qualitatively observed that, for $T = T_0$ and $\theta = 0^\circ$, the modified Hermite model provides the best
455 estimates of the experimental peak factors among all models considered here, closely followed by the
456 Liu's model. The TPP model identifies the regions of non-Gaussianity but generally underestimate the
457 peak factors, whereas the Davenport model severely underestimates the peak factors in the non-Gaussian
458 regions of the roof. All models provide very similar results that are close to the experimentally measured

459 peak factors in the middle and in the leeward edge of the roof (i.e., in zones D and E), where the pressure
 460 coefficient process can be approximately considered Gaussian.

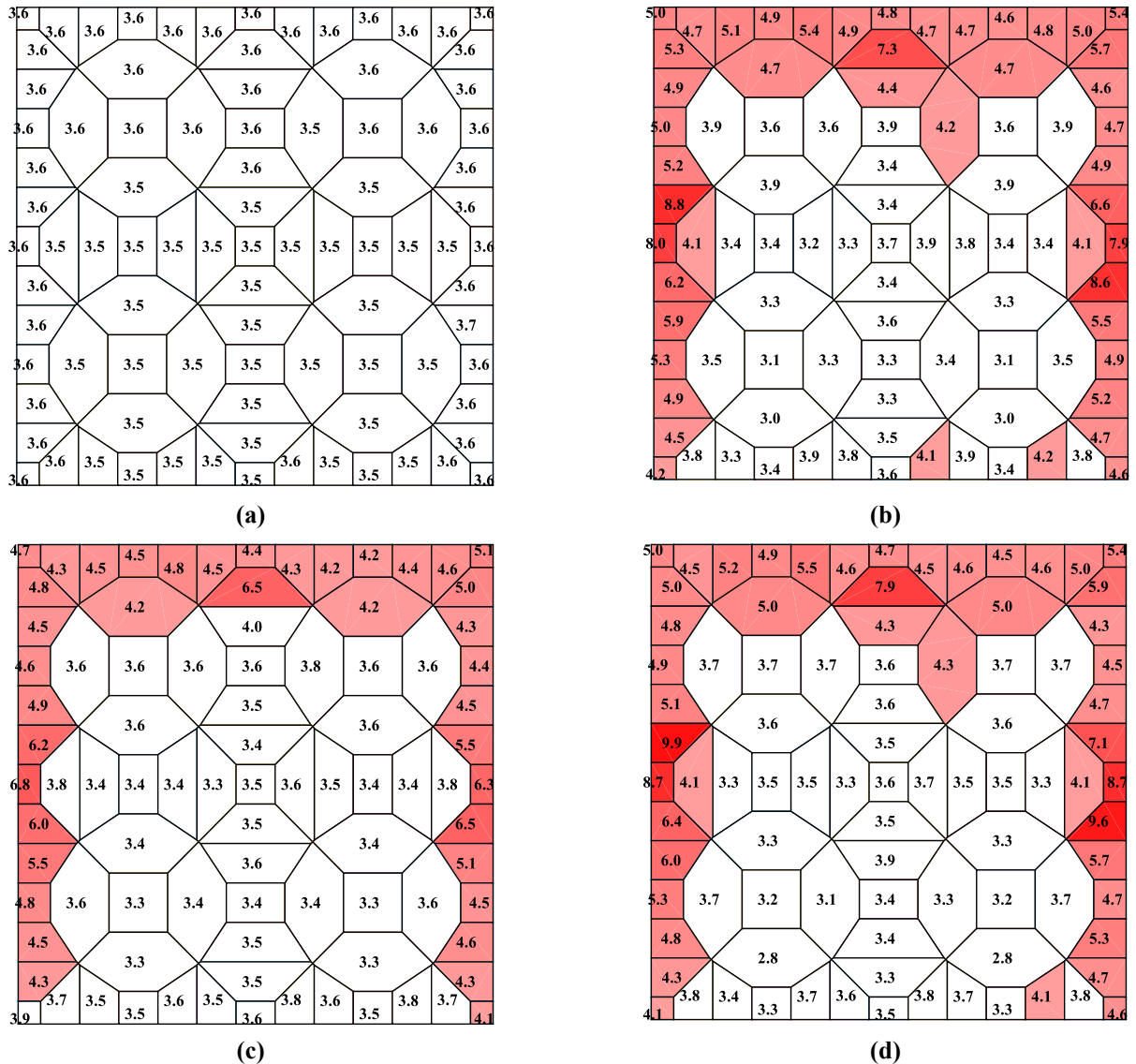


Figure 8. Analytical estimates of peak factor mean for $T = T_0$ and $\theta = 0^\circ$: (a) Davenport model, $\mu_{g,D}$;
 (b) modified Hermite model, $\mu_{g,mH}$; (c) TPP model, $\mu_{g,TPP}$; and (d) Liu's model, $\mu_{g,L}$

461 Figure 9 shows the analytical estimates of the peak factor standard deviation (scaled up by a factor equal
 462 to 10) corresponding to the Davenport, modified Hermite, TPP, and Liu's models for a time interval $T =$
 463 T_0 and wind angle $\theta = 0^\circ$. The Davenport estimates of the peak factor standard deviation at the different
 464 pressure taps are shown in Figure 9a. The standard deviation values change very little with the position

465 on the roof. The maximum and minimum values are equal to 0.389 and 0.367, respectively, which
466 correspond to coefficients of variation that are relatively small and slightly higher than 10%.

467 Figure 9b reports the peak factor standard deviation estimates obtained using the modified Hermite model.
468 Higher values for the standard deviation are observed near the highest points of the roof in zones B and
469 C (where also the peak factor mean is highest and the pressure coefficient process is strongly non-
470 Gaussian), whereas intermediate values are observed in zone A and the remainder of zones B and C, and
471 lower values are observed in most of zones D and E. The maximum value is equal to 2.121, with
472 coefficients of variation higher than 18% in highly non-Gaussian regions. The minimum value is equal
473 to 0.155.

474 The TPP estimates of the peak factor standard deviation are shown in Figure 9c. The peak factor standard
475 deviations have a trend similar to those of the modified Hermite model, but with a significantly smaller
476 range, i.e., with higher values in zones A, B, and C and lower values in zones D and E. The maximum
477 and minimum values of the peak factor standard deviations are equal to 1.107 and 0.338, respectively,
478 with coefficients of variation close to about 15% in highly non-Gaussian regions.

479 The Liu's estimates of the peak factor standard deviation are shown in Figure 9d. The peak factor standard
480 deviations have a trend similar to those of the modified Hermite and TPP models, but with larger
481 maximum values. The maximum and minimum values of the peak factor standard deviations are equal to
482 2.810 and 0.083, respectively.

483 Figure 10 compares the experimental values of the peak factors at each pressure tap with the
484 corresponding analytical estimates of the 90%-confidence intervals (defined as the interval between the
485 5% and 95% quantiles) of the peak factors for the Davenport, modified Hermite, TPP, and Liu's models.
486 The numbering of the pressure taps reported on the horizontal axis of Figure 10 corresponds to the
487 numbering shown in Figure 3. Vertical dashed lines are used to separate the pressure taps in the five
488 different zones identified as A, B, C, D, and E. The experimental peak factors are identified by red circular

489 markers for pressure taps corresponding to (approximately) Gaussian processes and by green square
 490 markers for pressure taps corresponding to non-Gaussian processes.

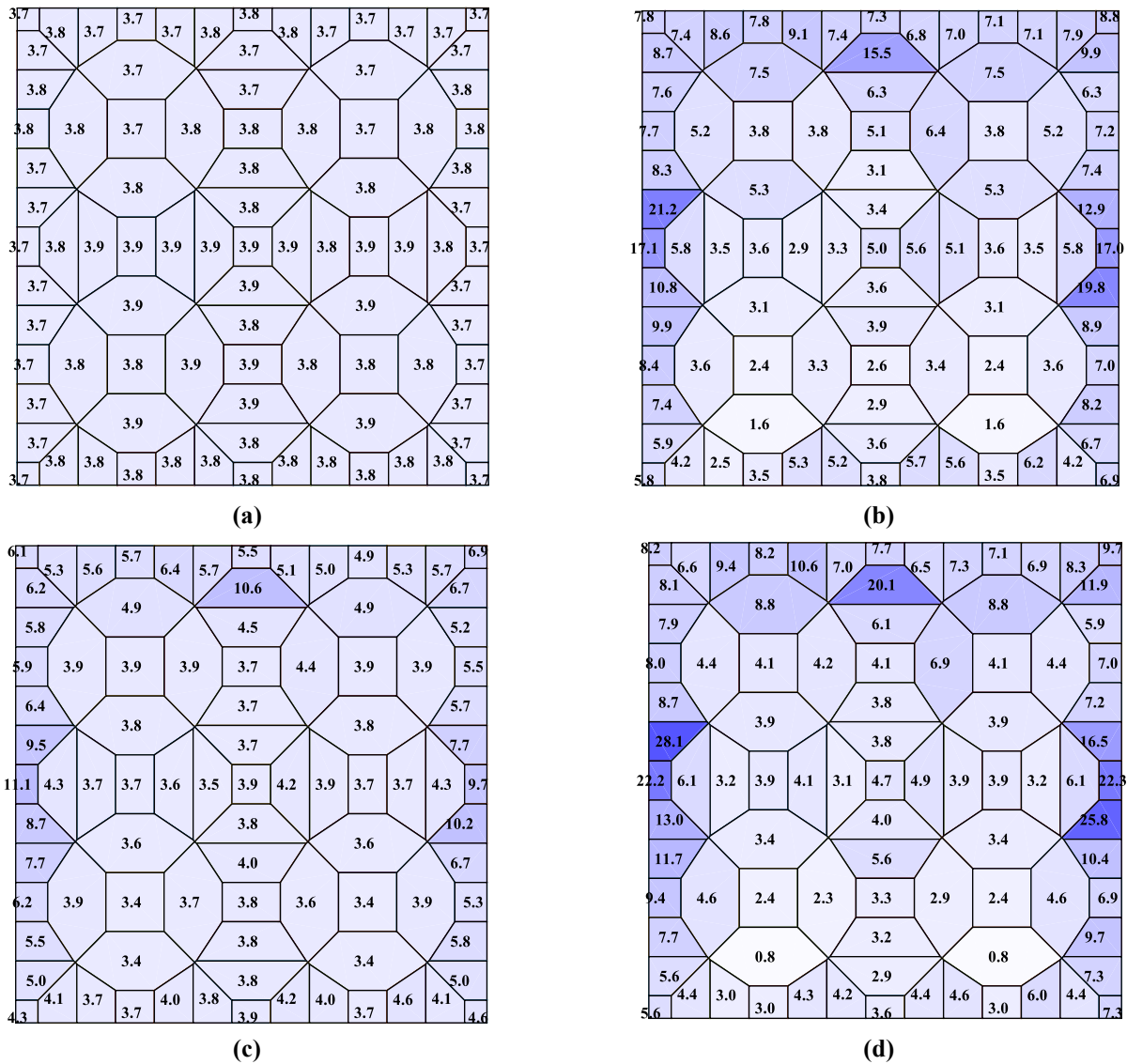


Figure 9. Analytical estimates of peak factor standard deviation, scaled up by 10, for $T = T_0$ and $\theta = 0^\circ$: (a) Davenport model, $\sigma_{g,D}$; (b) modified Hermite model, $\sigma_{g,mH}$; (c) TPP model, $\sigma_{g,TPP}$; and (d) Liu's model, $\sigma_{g,L}$

491 It is observed that the upper and lower bounds of the 90%-confidence intervals based on the Davenport
 492 model are almost constant, with the average value of the 5% quantiles equal to 3.088 and the average
 493 value of the 95% quantiles equal to 4.281. The modified Hermite model presents confidence intervals
 494 that are significantly wider than those obtained using the Davenport model in zones A, B, C, and a few
 495 pressure taps in zone E. These locations correspond to strongly non-Gaussian pressure coefficient

496 processes. In zone D and most of zone E (i.e., where the pressure coefficient processes are approximately
 497 Gaussian), the 90%-confidence intervals become very close to those estimated using the Davenport
 498 model. Similar observations are made for the TPP and Liu's models when compared to the Davenport
 499 model's results. The estimated quantiles are generally lower (particularly the 95% quantile) and the
 500 confidence intervals are generally narrower than those obtained from the modified Hermite model for the
 501 TPP model. By contrast, the Liu's model provides quantiles that are generally very close to those of the
 502 modified Hermite model, except for a few pressure taps where the pressure coefficient process is highly
 503 non-Gaussian, where the 95% quantile obtained from the Liu's model is significantly higher than those
 504 obtained from the modified Hermite model.

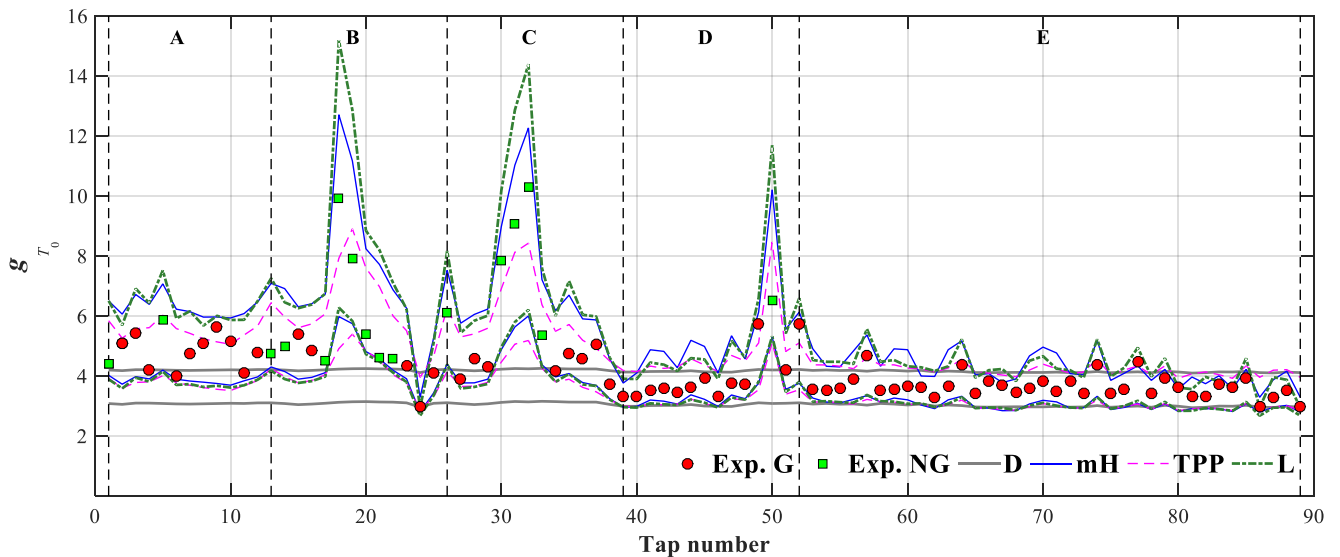


Figure 10. Comparison between experimental peak factors, g_{T_0} , and analytical peak factor 90%-confidence intervals for $T = T_0$ and $\theta = 0^\circ$.

505 6.1.2 Wind angle of attack $\theta = 45^\circ$

506 Similar to the case for $\theta = 0^\circ$, the analytical peak factor means and standard deviations were investigated
 507 also for $T = T_0$ and $\theta = 45^\circ$. The corresponding maps are not presented here due to space constraints.
 508 From these analytical estimates, it is observed that: (1) the Davenport model severely underestimates the
 509 peak factors in the non-Gaussian regions of the roof with very small differences of means and standard
 510 deviations in Gaussian and non-Gaussian regions; (2) the analytical peak factor means obtained using the

511 modified Hermite model provide the best estimates of the experimental peak factors; (3) the TPP model
512 can identify the regions of non-Gaussianity but generally underestimate the peak factors and have a
513 smaller range of variability of the standard deviations when compared to the Hermite models; (4) the
514 Liu's model gives a satisfactory identification of non-Gaussian regions but generally overestimate the
515 peak factors and presents the largest range of standard deviations. It is noteworthy that, while non-
516 Gaussianity is observed in most of the roof for $\theta = 45^\circ$, the values of the peak factors in these non-
517 Gaussian regions are generally lower than those for $\theta = 0^\circ$, which suggests a lower level of non-
518 Gaussianity.

519 Figure 11 compares the experimental peak factors for $T = T_0$ and $\theta = 45^\circ$ with the corresponding
520 analytical estimates of the 90%-confidence intervals of the peak factor at each pressure tap. Also in this
521 case, the 90%-confidence intervals based on the Davenport model are almost constant, significantly lower
522 than the experimental values in non-Gaussian regions, and close to those for $\theta = 0^\circ$. The Liu's model
523 generally presents wider 90%-confidence intervals when compared to other models, followed by the
524 modified Hermite and the TPP models. The modified Hermite, TPP, and Liu's models have significantly
525 wider 90%-confidence intervals than the Davenport model in zones A, B, C, and some parts of zone E
526 (i.e., where the pressure coefficient processes are non-Gaussian); whereas the 90%-confidence intervals
527 for all four models tend to similar values in zone D and the remainder of zone E (i.e., where the pressure
528 coefficient processes are approximately Gaussian). It is also observed that almost all experimental peak
529 factors are contained within the 90%-confidence intervals obtained using the modified Hermite and Liu's
530 models, whereas the TPP 90%-confidence intervals do not include a significant number of experimental
531 peak factors.

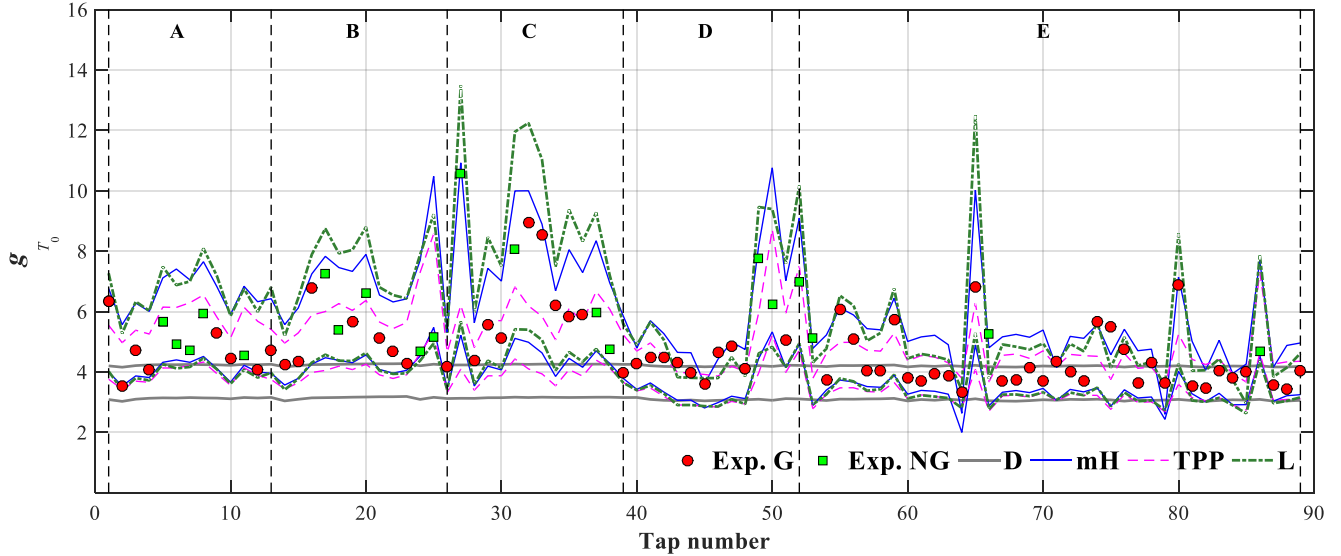


Figure 11. Comparison between experimental peak factors, g_{T_0} , and analytical peak factor 90%-confidence intervals for $T = T_0$ and $\theta = 45^\circ$.

532 6.1.3 Wind angle of attack $\theta = 90^\circ$

533 The analytical peak factor means and standard deviations obtained for $T = T_0$ and $\theta = 90^\circ$ lead to
 534 observations that are qualitatively similar to those made for $\theta = 0^\circ$ and $\theta = 45^\circ$. Also in this case, the
 535 corresponding maps are not presented here due to space constraints. As for the previous cases, the
 536 Davenport estimates of the peak factor mean are almost constant for all the pressure taps, with the
 537 maximum and minimum values that are equal to 3.679 and 3.486, respectively. The modified Hermite
 538 estimates of the peak factor mean are close to the experimentally measured peak factors, particularly in
 539 zone B, where the pressure coefficient processes are highly non-Gaussian, with a maximum value equal
 540 to 7.653 and a minimum value equal to 3.018. The TPP estimates of the peak factor mean are overall in
 541 good-to-fair agreement with the experimentally measured peak factors, with the exception of the highest
 542 peak factors, which are significantly underestimated by the TPP model. The maximum and minimum
 543 values of the peak factor mean based on the TPP model are equal to 6.397 and 3.140, respectively. The
 544 Liu's model gives estimates of the peak factor mean that are very close to and generally slightly higher
 545 than those of the modified Hermite model, with values ranging between 8.349 and 3.054.

546 Figure 12 compares the peak factor experimental values and the analytical estimates of the
 547 90%-confidence intervals of the peak factor at each pressure tap. Also in this case, the 90%-confidence
 548 intervals based on the Davenport model are almost constant and close to those for the other wind angles.
 549 As observed for other wind angles, the widths of the 90%-confidence intervals in non-Gaussian regions
 550 are generally largest for the Liu’s model, followed by the modified Hermite model and the TPP model,
 551 whereas they are smallest for the Davenport models, for which they are almost constant and close to those
 552 observed in Gaussian regions (i.e., most of region C). Almost all experimental peak factors are contained
 553 within the 90%-confidence intervals obtained using the modified Hermite and Liu’s models, whereas the
 554 90%-confidence intervals obtained using the TPP model fail to capture the largest values of the peak
 555 factors.

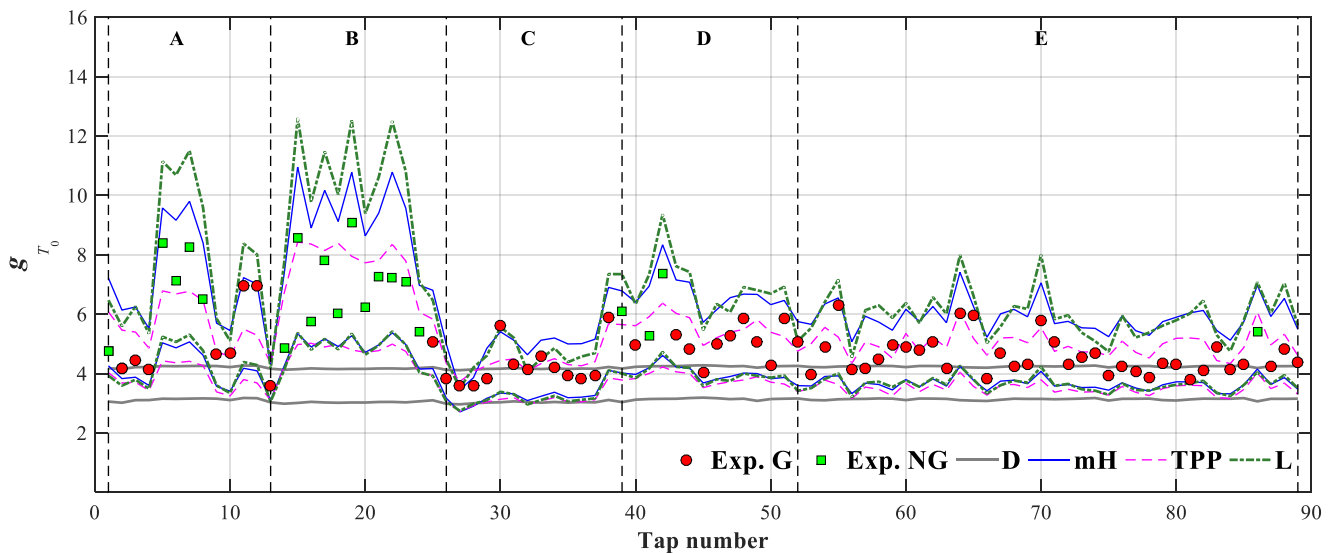


Figure 12. Comparison between experimental peak factors, g_{T_0} , and analytical peak factor 90%-confidence intervals for $T = T_0$ and $\theta = 90^\circ$.

556 6.1.4 Synoptic considerations for all wind angles

557 The empirical distributions of the pressure coefficient local peaks were investigated at all pressure taps
 558 for all wind angles in order to verify the assumptions made in the calculation of the confidence intervals
 559 for the peak factor, i.e., that the pressure coefficient local peaks follow a Rayleigh distribution in the
 560 Davenport model and that they follow a Weibull distribution in all other models. In all cases, a Rayleigh

561 and a Weibull distribution were fitted to the experimental data and a two-sided Kolmogorov-Smirnov test
 562 was performed [63].
 563 It was found that the Weibull distribution could not be rejected with a 5% confidence level in 251 cases
 564 out of 267 (i.e., in 94.0% of the cases), whereas the Rayleigh distribution was rejected with a 5%
 565 confidence level in all cases. Figure 13 plots the comparison between the empirical CDF and the fitted
 566 Rayleigh and Weibull distributions relative to the pressure coefficient local peaks for the case of pressure
 567 tap #19 and $\theta = 90^\circ$. This case corresponds to highly non-Gaussian conditions. It is observed that the
 568 Weibull distribution follows very well the empirical CDF, whereas the Rayleigh distribution shows
 569 significant differences with the empirical CDF.
 570 These observations confirm that the assumption that the pressure coefficient local peaks follow a Weibull
 571 distribution is reasonable. In addition, the Rayleigh distribution was found to differ significantly from the
 572 empirical CDF even for cases in which the pressure coefficient process could be considered
 573 approximately Gaussian.

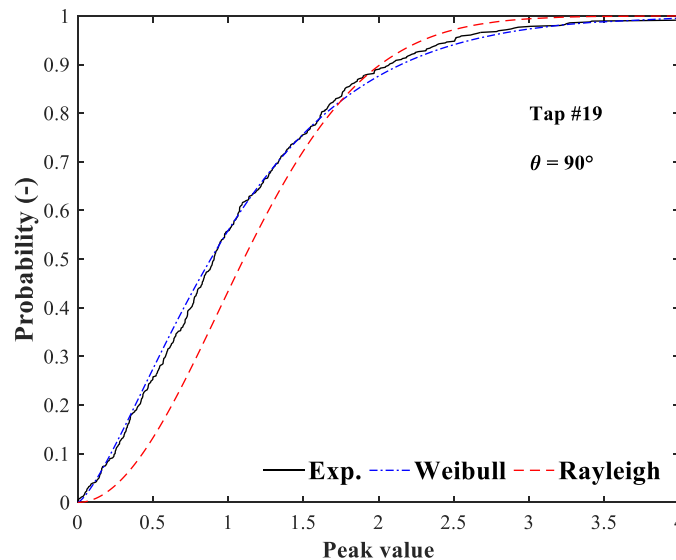


Figure 13. Cumulative distribution function (CDF) of pressure coefficient peaks at pressure tap #19 for $\theta = 90^\circ$ (highly non-Gaussian case).

574 When considering the entire duration of the records (i.e., for $T = T_0$), the experimental peak factors
 575 represent single realizations of random variables and cannot be directly compared with the peak factor

576 statistics (i.e., mean and standard deviation) obtained using the different analytical models considered in
577 this study. Thus, in order to provide a quantitative measure of the overall accuracy of the different
578 analytical models for the different wind angles, the analytical estimates of different quantiles $X_M^\alpha(T)$ were
579 compared with the recorded experimental values of the peak factors at each pressure tap. Table 1 reports
580 the ratios $R_M^\alpha(T)$ (expressed in percentage) of experimental peak factors (over all pressure taps for any
581 given wind angle) that are lower than the analytical quantiles $X_M^\alpha(T)$ for $T = T_0$, $M = D$, mH , TPP , and
582 L , and $\alpha = 95\%$, 75% , 50% , and 25% . The differences between these quantities and the corresponding α
583 values can be used as a proxy of the overall accuracy of each model in estimating the statistics of the peak
584 factors. In fact, the closer this ratio is to the corresponding value of α , the more accurate the corresponding
585 model can be considered in describing the actual distribution of the peak factors over the entire roof.
586 As expected, the Davenport model is the least accurate among the models investigated in this study. In
587 fact, the values of $R_D^\alpha(T_0)$ are always significantly lower than α and decrease with increasing wind angle.
588 The modified Hermite and Liu's models are the most accurate models, even though they tend to
589 overestimate the peak factor values, as indicated by the fact that the values of $R_{mH}^\alpha(T_0)$ and $R_L^\alpha(T_0)$ are
590 systematically higher than the corresponding α , with the only exception of the case for $\alpha = 25\%$ and $\theta =$
591 90° for the modified Hermite model. The TPP model tends to underestimate the peak factor values, as
592 indicated by the fact that $R_{TPP}^\alpha(T_0) < \alpha$ for all values of α and all wind angles.

593 Table 1. Ratios $R_M^\alpha(T_0)$ (in percentage) of experimental peak factors lower than $X_M^\alpha(T_0)$.

θ	D				mH				TPP				L			
	95%	75%	50%	25%	95%	75%	50%	25%	95%	75%	50%	25%	95%	75%	50%	25%
0°	57.3	39.3	15.7	2.2	100.0	85.4	74.2	57.3	87.6	61.8	32.6	6.7	100.0	93.3	68.5	27.0
45°	37.1	15.7	2.2	0.0	94.4	69.7	50.6	29.2	66.3	39.3	16.9	4.5	93.3	82.0	59.6	29.2
90°	28.1	4.5	0.0	0.0	98.9	75.3	39.3	12.4	70.8	32.6	10.1	1.1	100.0	94.4	66.3	25.8

594

595 **6.2 Comparison of peak factor statistics for $T < T_0$**

596 A comparison of the experimental and analytical peak factor statistics for time intervals that are shorter
597 than the entire pressure coefficients' records was performed to further investigate the relative accuracy of
598 the analytical models considered in this study. This additional comparison allows a direct comparison of
599 the peak factor's statistics evaluated using analytical models and experimental data.

600 Three smaller time interval lengths were considered, namely $T_1 = T_0/6 = 5$ s (corresponding to
601 approximately 300 s of equivalent-time duration for a full-scale structure), $T_2 = T_0/30 = 1$ s
602 (corresponding to approximately 60 s of equivalent-time duration for a full-scale structure) and $T_3 =$
603 $T_0/60 = 0.5$ s (corresponding to approximately 30 s of equivalent-time duration for a full-scale
604 structure). The lengths of the shorter intervals were selected so that the entire signal records could be
605 easily divided into a sufficient number of shorter signals of equal length (i.e., into sub-intervals), which
606 could provide reliable estimates of the experimental peak factor means and standard deviations. The
607 experimental peak factors were recorded for each sub-interval and were used to estimate at each pressure
608 tap the sample mean and standard deviation of the peak factor corresponding to the shorter signal duration,
609 based on six, 30, and 60 samples for T_1 , T_2 , and T_3 , respectively. It is noted here that the time intervals
610 considered in this study are shorter than those conventionally used to evaluate maximum wind pressures
611 in wind engineering practice (which are often 10-minute or 1-hour durations). However, the goal of the
612 present investigation is to investigate the relative accuracy of different analytical approximations for peak
613 factor statistics when considering different time durations, which can be achieved independently from the
614 specific values of the time durations considered. In fact, once the accuracy of a given analytical method
615 is verified over a range of different time durations, this analytical method can be used to estimate the
616 pressure coefficients corresponding to any time duration of interest with the same accuracy.

617 By comparing the analytical peak factor statistics of different models for different time durations, it is
618 observed that the peak factor mean increases monotonically for increasing time durations. The peak factor

619 standard deviation strictly decreases for increasing time durations everywhere for the Davenport model
 620 and in Gaussian regions for all other models, whereas the peak factor standard deviation does not have a
 621 monotonic behavior as a function of the time duration in regions of high non-Gaussianity for all models
 622 other than the Davenport model.

623 The overall accuracy of the different analytical models for the different wind angles was evaluated by
 624 estimating the following four different errors for the peak factor means and standard deviations:

625 (1) the average difference over all the pressure taps between the analytical and experimental estimates of
 626 means (ε_1) and standard deviations (δ_1), hereafter referred to as “average error”:

$$\varepsilon_1 = \frac{1}{89} \sum_{i=1}^{89} [\mu_{g,M}^{(i)}(T) - \mu_{g,\text{exp}}^{(i)}(T)] \quad (22)$$

$$\delta_1 = \frac{1}{89} \sum_{i=1}^{89} [\sigma_{g,M}^{(i)}(T) - \sigma_{g,\text{exp}}^{(i)}(T)] \quad (23)$$

627 (2) the root mean squared difference over all the pressure taps between the analytical and experimental
 628 estimates of means (ε_2) and standard deviations (δ_2), hereafter referred to as “root mean squared
 629 error” (RMSE):

$$\varepsilon_2 = \sqrt{\frac{1}{89} \sum_{i=1}^{89} [\mu_{g,M}^{(i)}(T) - \mu_{g,\text{exp}}^{(i)}(T)]^2} \quad (24)$$

$$\delta_2 = \sqrt{\frac{1}{89} \sum_{i=1}^{89} [\sigma_{g,M}^{(i)}(T) - \sigma_{g,\text{exp}}^{(i)}(T)]^2} \quad (25)$$

630 (3) the square root of the variation of the mean squared error proposed in [47] for means (ε_3) and standard
 631 deviations (δ_3), hereafter referred to as “modified root mean squared error” (mRMSE):

$$\varepsilon_3 = \sqrt{\frac{1}{89} \sum_{i=1}^{89} S_i^2} \quad (26)$$

$$\delta_3 = \sqrt{\frac{1}{89} \sum_{i=1}^{89} Z_i^2} \quad (27)$$

632 in which:

$$S_i = \begin{cases} \mu_{g,M}^{(i)}(T) - [\mu_{g,\text{exp}}^{(i)}(T) + 2SE_{\mu}^{(i)}] & \text{if } \mu_{g,M}^{(i)}(T) - \mu_{g,\text{exp}}^{(i)}(T) > 2SE_{\mu}^{(i)} \\ 0 & \text{if } |\mu_{g,M}^{(i)}(T) - \mu_{g,\text{exp}}^{(i)}(T)| \leq 2SE_{\mu}^{(i)} \\ \mu_{g,M}^{(i)}(T) - [\mu_{g,\text{exp}}^{(i)}(T) - 2SE_{\mu}^{(i)}] & \text{if } \mu_{g,M}^{(i)}(T) - \mu_{g,\text{exp}}^{(i)}(T) < -2SE_{\mu}^{(i)} \end{cases} \quad (28)$$

$$Z_i = \begin{cases} \sigma_{g,M}^{(i)}(T) - [\sigma_{g,\text{exp}}^{(i)}(T) + 2SE_{\sigma}^{(i)}] & \text{if } \sigma_{g,M}^{(i)}(T) - \sigma_{g,\text{exp}}^{(i)}(T) > 2SE_{\sigma}^{(i)} \\ 0 & \text{if } |\sigma_{g,M}^{(i)}(T) - \sigma_{g,\text{exp}}^{(i)}(T)| \leq 2SE_{\sigma}^{(i)} \\ \sigma_{g,M}^{(i)}(T) - [\sigma_{g,\text{exp}}^{(i)}(T) - 2SE_{\sigma}^{(i)}] & \text{if } \sigma_{g,M}^{(i)}(T) - \sigma_{g,\text{exp}}^{(i)}(T) < -2SE_{\sigma}^{(i)} \end{cases} \quad (29)$$

633 and $SE_{\mu}^{(i)}$ and $SE_{\sigma}^{(i)}$ denote the standard errors for the mean and standard deviation, respectively, at
 634 pressure tap i ;

635 (4) the percentage average error ratio over all the pressure taps used in [46] for means (ε_4) and standard
 636 deviations (δ_4), hereafter referred to as “percentage average error ratio” (PAER):

$$\varepsilon_4 = \frac{1}{89} \sum_{i=1}^{89} \frac{|\mu_{g,M}^{(i)}(T) - \mu_{g,\text{exp}}^{(i)}(T)|}{\mu_{g,\text{exp}}^{(i)}(T)} \cdot 100\% \quad (30)$$

$$\delta_4 = \frac{1}{89} \sum_{i=1}^{89} \frac{|\sigma_{g,M}^{(i)}(T) - \sigma_{g,\text{exp}}^{(i)}(T)|}{\sigma_{g,\text{exp}}^{(i)}(T)} \cdot 100\% \quad (31)$$

637 These errors were derived from the literature as they are representative of different selections made by
 638 different authors. It is noted here that: (1) only few studies in the literature consider the errors on the peak

639 factor standard deviations [42]; (2) only few studies investigate the overall accuracy of different models
640 on an entire roof [46], [47]; and (3) the authors were not able to identify any study in the literature that
641 compared the results obtained from different error definitions. The average errors and RMSE are those
642 more commonly used in the literature; however, they present some limitations. In particular, average
643 errors are intuitive and clearly indicate if a model tends to underestimate or overestimate the peak factor
644 statistics; however, they tend to cancel out large errors in opposite directions (i.e., underestimations and
645 overestimations) that are averaged out over many different pressure taps. RMSEs provide an average
646 difference between experimental and analytical results, which provide a better information on how
647 different are analytical and experimental results on the single pressure tap, but loses the information
648 regarding underestimations or overestimations. Both types of errors are affected by the quality of the
649 experimental data, i.e., by the number of samples available to estimate the sample mean and sample
650 standard deviations. The mRMSE was defined here by taking the square root of the error proposed in [47]
651 in order to obtain a quantity with the same dimensions of the average errors and the RMSEs. This error
652 measure minimizes the effects of small sampling size in the experimental data and, thus, can be considered
653 a more reliable error measure than average errors and RMSEs over different time durations. It is noted
654 here that the RMSEs tend to the mRMSEs when the experimental sampling size is sufficiently large.
655 Finally, the PAERs provide information on the relative errors, which is very intuitive but may be
656 misleading when the peak factor values vary over a wide range, e.g., in the case of roofs with both
657 approximately Gaussian and highly non-Gaussian regions such as those considered in this study.
658 Table 2 reports the peak factor mean's error statistics averaged over all pressure taps for the different time
659 intervals, wind angles, and models considered in this study. For each case, the smallest error in absolute
660 value is highlighted in bold fonts. It is observed that all methods tend to underestimate the overall peak
661 factor means (as indicated by the negative values of the average errors for all time intervals and wind
662 angles), and this underestimation is most severe in the case of the Davenport model, as expected. The

663 modified Hermite and Liu's models appear to be similarly accurate when considering the average error;
664 however, when other error measures are considered, these errors for the Liu's model are significantly
665 larger than those for the modified Hermite model and are comparable to or slightly higher than those
666 obtained using the TPP model. The PAER are contained between 5.0% and 9.2% for the modified
667 Hermite, TPP, and Liu's models, indicating an accuracy generally acceptable for engineering
668 applications; whereas they are larger for the Davenport model, with values contained between 12.8% and
669 20.5%. Overall, the modified Hermite model is observed to provide the best estimates of the peak factor
670 means in almost all cases according to all error measures. However, different error measures appear to
671 provide different indications on the relative accuracy of the different models for different time durations,
672 e.g., by looking at average errors alone, it would be difficult to identify which model between the modified
673 Hermite and Liu's ones is most accurate. It also appears that the mRMSE is the most consistent, among
674 the error measures considered in this study, in identifying the modified Hermite model as the most
675 accurate model overall. Finally, the errors for $\theta = 45^\circ$ are consistently higher than those for other angles
676 for each error measure considered here.

677 Table 2. Peak factor mean's error statistics averaged over all pressure taps for $T = T_1, T_2,$ and T_3 .

		T	θ	D	mH	TPP	L
ε_1 Average error	T_1		0°	-0.579	-0.027	-0.186	-0.037
			45°	-0.732	-0.015	-0.295	-0.011
			90°	-0.858	-0.012	-0.296	0.017
	T_2		0°	-0.376	-0.056	-0.140	-0.070
			45°	-0.444	-0.046	-0.183	-0.054
			90°	-0.509	-0.042	-0.183	-0.040
	T_3		0°	-0.342	-0.104	-0.176	-0.115
			45°	-0.375	-0.083	-0.191	-0.091
			90°	-0.402	-0.061	-0.180	-0.060
ε_2 RMSE	T_1		0°	0.873	0.236	0.335	0.252
			45°	0.885	0.365	0.475	0.442
			90°	1.024	0.250	0.390	0.317
	T_2		0°	0.444	0.224	0.201	0.247
			45°	0.491	0.253	0.273	0.298
			90°	0.551	0.197	0.229	0.227
	T_3		0°	0.367	0.227	0.217	0.243
			45°	0.391	0.236	0.254	0.265
			90°	0.417	0.196	0.214	0.216
ε_3	T_1		0°	0.400	0.045	0.039	0.045
			45°	0.326	0.136	0.169	0.151

mRMSE	T_2	90°	0.445	0.036	0.082	0.032	
		0°	0.243	0.087	0.092	0.099	
		45°	0.275	0.123	0.153	0.150	
	T_3	90°	0.311	0.056	0.097	0.069	
		0°	0.227	0.125	0.128	0.137	
		45°	0.241	0.138	0.163	0.163	
	ε_4 PAER	T_1	90°	0.256	0.077	0.111	0.092
			0°	14.2%	5.6%	6.5%	5.6%
			45°	18.0%	6.7%	9.2%	8.3%
T_2		90°	20.5%	5.0%	7.8%	6.2%	
		0°	12.8%	6.7%	6.4%	7.1%	
		45°	14.7%	6.7%	7.2%	7.7%	
T_3		90°	16.6%	5.4%	6.6%	6.1%	
		0°	13.5%	7.9%	7.9%	8.4%	
		45°	14.3%	7.4%	8.0%	8.3%	
		90°	15.3%	6.4%	7.3%	7.0%	

678 Table 3 reports the peak factor standard deviation's error statistics averaged over all pressure taps for the
679 different time intervals, wind angles, and models considered in this study. For each case, the smallest
680 error in absolute value is highlighted in bold fonts.

681 Table 3. Peak factor standard deviation's error statistics averaged over all pressure taps for $T = T_1, T_2,$ and T_3 .

	T	θ	D	mH	TPP	L
δ_1 Average error	T_1	0°	-0.087	0.152	0.037	0.188
		45°	-0.275	0.075	-0.136	0.114
		90°	-0.305	0.109	-0.118	0.179
	T_2	0°	-0.017	0.203	0.112	0.234
		45°	-0.122	0.192	0.022	0.226
		90°	-0.168	0.205	0.025	0.265
	T_3	0°	0.207	0.298	0.217	0.329
		45°	0.189	0.283	0.130	0.317
		90°	0.149	0.301	0.140	0.362
δ_2 RMSE	T_1	0°	0.438	0.257	0.316	0.271
		45°	0.552	0.327	0.448	0.287
		90°	0.545	0.277	0.363	0.297
	T_2	0°	0.311	0.210	0.196	0.254
		45°	0.296	0.230	0.199	0.282
		90°	0.328	0.214	0.144	0.293
	T_3	0°	0.267	0.297	0.236	0.353
		45°	0.225	0.297	0.191	0.361
		90°	0.222	0.302	0.159	0.394
δ_3 mRMSE	T_1	0°	0.095	0.109	0.079	0.113
		45°	0.094	0.140	0.081	0.117
		90°	0.079	0.105	0.054	0.137
	T_2	0°	0.172	0.098	0.075	0.103
		45°	0.140	0.119	0.071	0.115
		90°	0.165	0.091	0.029	0.120
	T_3	0°	0.171	0.194	0.147	0.241
		45°	0.122	0.188	0.102	0.243
		90°	0.120	0.180	0.075	0.267
		0°	55.7%	59.2%	54.5%	56.8%

δ_4 PAER	T_1	45°	46.0%	56.5%	44.8%	49.7%
		90°	39.7%	47.5%	35.5%	49.2%
	T_2	0°	32.9%	38.5%	31.5%	39.9%
		45°	28.7%	34.2%	24.5%	36.8%
		90°	23.4%	32.3%	17.1%	36.9%
	T_3	0°	35.2%	50.6%	42.1%	52.9%
		45°	28.4%	44.2%	29.2%	46.8%
		90°	18.4%	43.3%	22.9%	48.6%

682 It is observed that the Davenport model mostly underestimates the peak factor standard deviations, as
683 indicated by the predominant negative values of the corresponding average errors, whereas the modified
684 Hermite and Liu's models tend to overestimate overall the peak factor standard deviations. By comparing
685 the results corresponding to all error measures, the TPP model appears to provide the best overall
686 estimates of the peak factor standard deviations. However, similar to the observations made for the peak
687 factor mean's errors, different error measures give somewhat different indications on the relative accuracy
688 of the different models for different time durations. For example, the PAER indicates that the Davenport
689 model is the most accurate model overall in estimating the peak factor standard deviation for $T = T_3$,
690 which is a counterintuitive and potentially misleading conclusion. In fact, after a closer inspection of the
691 relative absolute errors at each single pressure tap, it was concluded that this result stems from the fact
692 that the PAER systematically discounts the errors in highly non-Gaussian regions (which are larger for
693 the Davenport model when compared to the other models) and amplifies the errors in approximately
694 Gaussian regions (which are similar among different models). Also in this case, the mRSME appears to
695 provide the most consistent results. Thus, it is suggested that the mRSME should be used when comparing
696 the results obtained from different models over a large number of pressure taps, particularly when a small
697 sample size is used to estimate experimentally the statistics of the pressure coefficient peak factors.

698 7 Conclusions

699 This paper investigates the statistics of the pressure coefficients and their peak factors in hyperbolic
700 paraboloid roofs (HPRs), with particular attention to the characterization of the non-Gaussian properties
701 of the peak factors as functions of the position on a square HPR and the relative direction of the wind.

702 Experimental results for wind tunnel tests on a scaled model of a building with a square HPR are reported
703 for three different wind angles of attack (i.e., $\theta = 0^\circ$, 45° , and 90°).

704 The pressure coefficient processes at different locations on the roof were identified as (approximately)
705 Gaussian or non-Gaussian based on the values of their skewness coefficient and excess kurtosis. For $\theta =$
706 0° (i.e., for a wind angle of attack parallel to the hogging direction of the roof), the pressure coefficient
707 processes were identified as non-Gaussian along the detachment edge and the two edges that are parallel
708 to the direction of the wind, and as approximately Gaussian elsewhere. The largest values of the skewness
709 coefficients and excess kurtosis were achieved near the highest points of the roof, i.e., near the middle of
710 the two edges parallel to the direction of the wind. For $\theta = 45^\circ$ (i.e., for a wind direction that is incident
711 to the corner of the roof), the pressure coefficient processes were classified as non-Gaussian along the
712 two detachment edges (one parallel to the hogging and the other to the sagging direction), along the other
713 edge parallel to the sagging direction, and in a significant portion of the interior of the roof close to the
714 two detachment edges. For $\theta = 90^\circ$ (i.e., for a wind direction that is parallel to the sagging direction of
715 the roof), the pressure coefficient processes were highly non-Gaussian along the detachment edge and the
716 two edges parallel to the wind directions, had a non-negligible level of non-Gaussianity in approximately
717 half of the interior of the roof (i.e., behind the detachment edge until approximately the middle of the
718 roof), and were approximately Gaussian elsewhere. These observations were confirmed by the values of
719 the experimental peak factors obtained from the entire record duration $T = T_0 = 30$ s (corresponding to
720 approximately 30 min of pressure coefficient's record for a full-scale structure), which were significantly
721 higher in the regions identified as non-Gaussian than in those identified as approximately Gaussian for
722 all considered wind angles.

723 The analytical estimates of peak factors' statistics were calculated and compared with the corresponding
724 experimental estimates by using six different analytical models, namely, the Davenport (D), classical
725 Hermite (H), revised Hermite (rH), modified Hermite (mH), Translated-Peak-Process (TPP), and Liu's

726 (L) models. This investigation directly compared the experimental and analytical estimates of different
727 quantiles for the entire duration of the experimental records. It was observed that the modified Hermite
728 and the Liu's models generally provided the most accurate estimates of the peak factors' quantiles,
729 whereas the TPP model generally slightly underestimated the peak factors values and the Davenport
730 model strongly underestimated the peak factors values. Based on the results of a two-sided Kolmogorov-
731 Smirnov test, it was also shown that that the pressure coefficient local peaks (i.e., the local maxima in
732 time of the pressure coefficient's experimental records) generally followed a Weibull distribution,
733 whereas the Rayleigh distribution was found to differ significantly from the empirical cumulative
734 distribution function even for cases in which the pressure coefficient process could be considered
735 approximately Gaussian.

736 Finally, the experimental and analytical peak factor means and standard deviations were compared for
737 three different time durations obtained by subdividing the experimental records into smaller subintervals.
738 The accuracy of the analytical estimates was investigated for three different wind angles of attack and
739 four different error measures. It was observed that the modified Hermite model provided the most accurate
740 estimates of the peak factor means overall, whereas the TPP model presented the most accurate estimates
741 of the peak factor standard deviations overall. It was also observed that different error measures could
742 lead to different (sometimes conflicting) conclusions when investigating different time durations. Among
743 the different error measures considered in this study, the modified root mean squared error appeared to
744 be the most reliable error measure, because it was able to reduce the effects of limited experimental
745 sample sizes on the accuracy of the experimental estimates of peak factor means and standard deviations.
746 Thus, it is suggested to use this error measure when assessing the accuracy of analytical models to
747 estimate the peak factor statistics over different pressure taps.

748 The study presented in this paper represents a first step toward the definition of appropriate ranges and
749 calculation methods for peak factors to be employed in the analysis and design of HPRs commonly used

750 as cost-effective tensile structures. The present research investigated the peak factor statistics only for a
751 single geometry (square roof) under a specified turbulence condition. Further research is needed to
752 generalize the conclusions reported in this paper, e.g., to different geometrical configurations (e.g., roof
753 curvature and building height), different shapes (e.g., rectangular and circular footprints), and different
754 turbulence conditions.

755 **Acknowledgements**

756 The second author would like to thank Professor Enrico Spacone and the University of Chieti-Pescara
757 “G. D’Annunzio” for partial support of this research during his stay in Pescara (Italy) for his sabbatical
758 leave in 2016. The present research was partially supported by the University “G. D’Annunzio” of Chieti-
759 Pescara (ex-60% funds) and by the National Science Foundation through award CMMI #1537078. Any
760 opinions, findings, conclusions or recommendations expressed in this publication are those of the authors
761 and do not necessarily reflect the views of the sponsors.

762 **References**

- 763 [1] Brandt J., Vejre H., 2004. Multifunctional landscapes: motives, concepts and perceptions. In J. Brandt & H. Vejre
764 (Eds.), *Multifunctional Landscapes*, Southampton, MA: WIT Press, 1, 3–33.
- 765 [2] Majowiecki M., 2004. *Tensostrutture: Progetto e Controllo*. (In Italian). Edizioni Crea, Milan (Italy).
- 766 [3] Chilton J., 2010. Tensile structures-textiles for architecture and design. In: Pöhl G. ed. *Textile Polymers and Composites*
767 *for Buildings*. Woodhead Publishing Limited, Cambridge (UK), 229–257
- 768 [4] Beccarelli P., 2015. *Biaxial Testing for Fabrics and Foils*. PoliMI Springer Briefs, DOI 10.1007/978-3-319-02228-4_2.
- 769 [5] CEN, 2005b. *EN 13782: Temporary Structures-Tent-Safety*. Comité Européen de Normalization (CEN), Brussels
770 (Belgium).
- 771 [6] ASCE, 2010b. *ASCE/SEI 19-16: Structural Applications of Steel Cables for Buildings*. American Society of Civil
772 Engineers (ASCE), Reston, VA (USA).
- 773 [7] ASCE, 2010c. *ASCE/SEI 55-10: Tensile Membrane Structures*. American Society of Civil Engineers (ASCE), Reston,
774 VA (USA).
- 775 [8] Huntington C.G., 2004. *The Tensioned Fabric Roof*. American Society of Civil Engineers (ASCE), Reston, VA (USA).
- 776 [9] Huntington C.G., 2013. *Tensile Fabric Structures. Design, Analysis, and Construction*. American Society of Civil
777 Engineers (ASCE), Reston, VA (USA).

- 778 [10] Foster B., Mollaert M., 2004. *The European Design Guide for Tensile Surface Structures*. TensiNet, Brussels (Belgium).
- 779 [11] McAlester V., McAlester L., 2013. *A Field Guide to American Houses*. New York (NY): Alfred and Knopf.
- 780 [12] Strode W., Dean D.L., 1958. Design, construction and testing of a plywood hyperbolic paraboloid lattice structure, *The*
781 *Bulletin of Engineering and Architecture*, **41**. Lawrence MA, University of Kansas Publications.
- 782 [13] Scotta R., Lazzari M., Stecca E., Cotela J., Rossi R., 2016. Numerical wind tunnel for aerodynamic and aeroelastic
783 characterization of bridge deck sections. *Computers and Structures*, **167**, 96–114.
- 784 [14] Rizzo F., Sepe V., 2015. Static loads to simulate dynamic effects of wind on hyperbolic paraboloid roofs with square plan.
785 *Journal of Wind Engineering & Industrial Aerodynamics*, **137**, 46-57.
- 786 [15] Vassilopoulou I., Gantes C.J., 2010. Nonlinear dynamic phenomena in a SDOF model of cable net. *Archive of Applied*
787 *Mechanics*, **82**(10-11), 1689-1703.
- 788 [16] Vassilopoulou I., Gantes C.J., 2011. Nonlinear dynamic behavior of saddle form cable nets under uniform harmonic load.
789 *Engineering Structures*, **33**(10), 2762-2771.
- 790 [17] Vassilopoulou I., Gantes C.J., 2012. Vibration modes and natural frequencies of saddle form cable nets. *Computers and*
791 *Structures*, **88**(1-2), 105-119.
- 792 [18] Vassilopoulou I., Petrini F., Gantes C.J., 2017. Nonlinear dynamic behavior of cable nets subjected to wind loading.
793 *Structures* **10**, 170–183. DOI: 10.1016/j.istruc.2017.03.004.
- 794 [19] Rizzo F., D’Asdia P., Lazzari M., Procino L., 2011. Wind action evaluation on tension roofs of hyperbolic paraboloid
795 shape. *Engineering Structures*, **33**(2), 445–461.
- 796 [20] Rizzo F., D’Asdia P., Ricciardelli F., Bartoli, G., 2012. Characterization of pressure coefficients on hyperbolic paraboloid
797 roofs. *Journal of Wind Engineering and Industrial Aerodynamics*, **102**, 61–71.
- 798 [21] Ding J., Chen X., 2014. Assessment of methods for extreme value analysis of non-Gaussian wind effects with short-term
799 time history samples. *Engineering Structures*, **80**, 75-88
- 800 [22] Rizzo F., 2014. *Aerodynamic Behavior of Tension Structures*. Silvana Editoriale, Milano (Italy).
801 ISBN/EAN:9788836628407.
- 802 [23] Liu M., Chen X., Yang Q., 2016. Characteristics of dynamic pressures on a saddle type roof in various boundary layer
803 flows. *Journal of Wind Engineering and Industrial Aerodynamics*, **150**, 1–14.
- 804 [24] Liu M., Chen X., Yang Q., 2017. Estimation of peak factor of non-Gaussian wind pressures by improved moment-based
805 Hermite model. *Journal of Engineering Mechanics*, **143**(7): 06017006.
- 806 [25] Rizzo F., Ricciardelli F., 2017. Design approach of wind load for Hyperbolic paraboloid roof with circular and elliptical
807 plan. *Engineering Structures*, **139**, 153-169.
- 808 [26] Caracoglia L., Zuo D., 2009. Effectiveness of Cable Networks of Various Configurations in Suppressing Stay-Cable
809 Vibration. *Engineering Structures*, **31**(12), 2851-2864.
- 810 [27] Kwon D., Kareem A., 2011. Peak Factors for Non-Gaussian Load Effects Revisited. *Journal of Structural Engineering*,
811 **137**(12), 1611-1619.
- 812 [28] Ciampoli M., Petrini F., 2012. Performance-based Aeolian risk assessment and reduction for tall buildings. *Probabilistic*
813 *Engineering Mechanics*, **28**, 75–84.

- 814 [29] Giaralis A., Petrini F. (2017). Wind-induced vibration mitigation in tall buildings using the tuned mass-damper-inerter.
815 *Journal of Structural Engineering ASCE*, **143**(9), 04017127, DOI: 10.1061/(ASCE)ST.1943-541X.0001863.
- 816 [30] Barbato M., Petrini F., Unnikrishnan V.U., Ciampoli M., 2013. Performance-based hurricane engineering (PBHE)
817 framework. *Structural Safety*, 45, 24–35.
- 818 [31] Gumbel E.J., 1958. *Statistics of Extremes*. Columbia University Press, New York, NY (USA).
- 819 [32] Davenport A.G., 1964. Note on the distribution of the largest value of a random function with application to gust loading.
820 *Proceedings of the Institution of Civil Engineering*, **28**(2), 187–196.
- 821 [33] Gurley K.R., Tognarelli M.A., Kareem A., 1997. Analysis and simulation tools for wind engineering. *Probabilistic*
822 *Engineering Mechanics*, **12**(1), 9–31.
- 823 [34] Kareem A., Zhao J., 1994. Analysis of non-Gaussian surge response of tension leg platforms under wind loads. *Journal*
824 *of Offshore Mechanics and Arctic Engineering*, **116**(3), 137-144.
- 825 [35] Winterstein S.R., 1988. Nonlinear vibration models for extremes and fatigue. *Journal of Engineering Mechanics*, **114**(10),
826 1772-1790.
- 827 [36] Grigoriu M., 1984. Crossings of non-Gaussian translation processes. *Journal of Engineering Mechanics*, **110**(4), 610-620.
- 828 [37] Winterstein S.R., Ude T.C., Kleiven, G., 1994. Springing and slow-drift responses: predicted extremes and fatigue vs
829 simulation. *Proceedings, Behavior of Offshore Structures at Sea - BOSS-94*, MIT, **3**, 1-15.
- 830 [38] Sadek F., Simiu E., 2002. Peak non-Gaussian wind effects for database-assisted low-rise building design. *Journal of*
831 *Engineering Mechanics*, **128**(5), 530-539.
- 832 [39] Tieleman H.W., Ge Z., Hajj M.R., 2007. Theoretically estimated peak wind loads. *Journal of Wind Engineering and*
833 *Industrial Aerodynamics*, **95**(2), 113–132.
- 834 [40] Tieleman H.W., Elsayed M.A.K., Ge Z., Hajj M.R., 2008. Extreme value distributions for peak pressure and load
835 coefficients. *Journal of Wind Engineering and Industrial Aerodynamics* **96**(6–7), 1111–1123.
- 836 [41] Choi M., Sweetman B., 2010. The Hermite moment model for highly skewed response with application to tension leg
837 platforms. *Journal of Offshore Mechanics and Arctic Engineering*, **132**(2), 021602.
- 838 [42] Huang M.F., Lou W., Chan C.M., Lin N., Pan X., 2013. Peak distributions and peak factors of wind-induced pressure
839 processes on tall buildings. *Journal of Engineering Mechanics*, **139**(12), 1744-1756.
- 840 [43] Seo D.W., Caracoglia L., 2010. Derivation of equivalent gust effect factors for wind loading on low-rise buildings through
841 Database-Assisted-Design approach. *Engineering Structures*, **32**(1), 328-336.
- 842 [44] Winterstein S.R., Kashef T., 2000. Moment-based load and response models with wind engineering applications. *Journal*
843 *of Solar Energy Engineering*, **122**, 122-128.
- 844 [45] Tognarelli M.A., Zhao J., Kareem A., 1997. Equivalent statistical cubicization for system and forcing nonlinearities.
845 *Journal of Engineering Mechanics*, **123**(8), 1772-1790.
- 846 [46] Ma X., Xu F., 2017. Peak factor estimation of non-Gaussian wind pressure on high-rise buildings. *The Structural Design*
847 *of Tall and Special Buildings*, **26**(17):e1386.
- 848 [47] Peng X., Yang L., Gavanski E., Gurley K., Prevatt D., 2014. A comparison of methods to estimate peak wind loads on
849 buildings. *Journal of Wind Engineering & Industrial Aerodynamics*, **126**, 11–23.

- 850 [48] AS/NZS, 2002. *AS/NZS 1170.2:2002: Structural Design Actions, Part 2: Wind actions*. Jointly published by Standards
851 Australia, Sydney (Australia) and Standards New Zealand, Wellington (New Zealand).
- 852 [49] SSEA, 2003. *Swiss Standard 505 261: Actions on Structures -Appendix C: Force and Pressure Factors for Wind*. Swiss
853 Society of Engineers and Architects (SSEA), Zurich (Switzerland).
- 854 [50] AIJ, 2004. *AIJ: Recommendations for Loads and Building with Commentaries, Chapter 6: Wind Loads*. Architectural
855 Institute of Japan (AIJ), Tokyo (Japan).
- 856 [51] CEN, 2005a. *EN1991-1-4: Eurocode1: Actions on structures - Part 1-4: General Actions, Wind Actions*. Comité
857 Européen de Normalization (CEN), Brussels (Belgium).
- 858 [52] ASCE, 2010a. *ASCE 7-10: Minimum Design Loads for Buildings and Other Structures*. American Society of Civil
859 Engineers (ASCE), Reston, VA (USA).
- 860 [53] NRCC, 2010. *NBCC-4.1.7: Commentary - Wind Load and Effects*. National Research Council of Canada (NRCC),
861 Ottawa, Ontario (Canada).
- 862 [54] CNR, 2011. *CNR-DT207: Guide for the Assessment of Wind Actions and Effects on Structures*. National Research Council
863 of Italy (CNR), Rome (Italy).
- 864 [55] ESA, 2012. *ES ISO 4354: Wind Action on Structures – D.3: Wind Tunnel Testing Procedures*. Ethiopian Standards
865 Agency (ESA), Addis Abeba (Federal Democratic Republic of Ethiopia).
- 866 [56] BIS, 2012. *IS 875: Code of Practice for Design Loads for Buildings and Structures -Proposed Draft & Commentary,*
867 *Part3: Wind Loads on Buildings*. Bureau of Indian Standards (BIS), New Delhi (India).
- 868 [57] Luo Y., Huang G., Ding J., Gurley K.R., 2016. Response to “Revisiting moment-based characterization for wind
869 pressures” by G. Huang, Y. Luo, K.R. Gurley and J. Ding. *Journal of Wind Engineering and Industrial Aerodynamics*,
870 **158**, 162–163
- 871 [58] Huang M.F., Huang S., Feng H., Lou W.J., 2016. Non-Gaussian time-dependent statistics of wind pressure processes on
872 a roof structure. *Wind and Structures*, **23**(4), 275-300.
- 873 [59] Suresh Kumar K., Stathopoulos T., 2000. Wind loads on low building roofs: a stochastic perspective. *Journal of Structural*
874 *Engineering*, **126**(8), 944-956.
- 875 [60] Cartwright D.E., Longuet-Higgins M.S., 1956. Statistical distribution of the maxima of a random function. *Proceedings*
876 *of the Royal Society of London. Series A, Mathematical and Physical Sciences*, **237**(1209), 212-232.
- 877 [61] Yang L., Gurley K.R., Prevatt D.O., 2013. Probabilistic modeling of wind pressure on low-rise buildings. *Journal of Wind*
878 *Engineering and Industrial Aerodynamics*, **114**, 18–26.
- 879 [62] Winterstein S.R., MacKenzie C.A., 2012. Extremes of nonlinear vibration: comparing models based on moments, l-
880 moments, and maximum entropy. *Journal of Offshore Mechanics and Arctic Engineering*, **135**(2):021602.
- 881 [63] Massey F.J., 1951. The Kolmogorov-Smirnov test for goodness of fit. *Journal of the American Statistical Association*,
882 **46**(253), 68-78.
- 883